Charles University in Prague
Faculty of Mathematics and Physics

MASTER'S THESIS

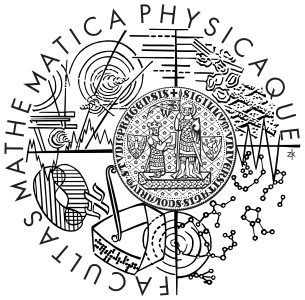

Ina Chalupková

Study of rare B decays in ATLAS

Institute of Particle and Nuclear Physics

Supervisor: doc. RNDr. Zdeněk Doležal, Dr.
Consultant: Mgr. Pavel Řezníček

Study programme: Physics
Specialization: Nuclear and Subnuclear Physics

2010

Univerzita Karlova v Praze
Matematicko-fyzikální fakulta

DIPLOMOVÁ PRÁCE

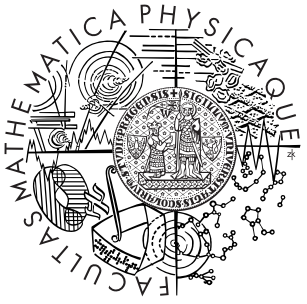

Ina Chalupková

Studium vzácných B rozpadů v detektoru ATLAS

Ústav částicové a jaderné fyziky

Vedoucí diplomové práce: doc. RNDr. Zdeněk Doležal, Dr.
Konzultant: Mgr. Pavel Řezníček

Studijní program: Fyzika
Obor: Jaderná a subjaderná fyzika

2010

I would like to thank my supervisor Zdeněk Doležal for his valuable comments and my consultant Pavel Řezníček for his helpful explanations of rare B decays, data analysis framework and results interpretation. Also many thanks to my family who have always supported me and Samu for motivating me.

Thank you, grazie, ďakujem.

I declare that I wrote my master's thesis independently and exclusively with the use of the cited sources. I agree with lending and publishing the thesis.

Prohlašuji, že jsem svou diplomovou práci napsala samostatně a výhradně s použitím citovaných pramenů. Souhlasím se zapůjčováním práce.

In Prague, 29. 7. 2010 Ina Chalupková

Contents

Název práce: Studium vzácných B rozpadů v detektoru ATLAS
Autor: Ina Chalupková
Katedra (Ústav): Ústav částicové a jaderné fyziky
Vedoucí diplomové práce: doc. RNDr. Zdeněk Doležal, Dr.
Konzultant: Mgr. Pavel Řezníček
e-mail vedoucího: dolezal@ipnp.troja.mff.cuni.cz

Abstrakt: V tejto práci analyzujeme riedky semileptonový rozpad $B_s^0 \to \phi^0 \mu^+ \mu^-$ v experimente ATLAS v CERN. Monte Carlo dáta sme spracovali pomocou offline algoritmu a navrhli optimalizované hodnoty parametrov filtrov, ktoré budú použité na výber signálnych prípadov. Spočítali sme účinnosť výberu, faktory potlačenia pozadia a odhadli predpokladaný počet prípadov v dátach s integrovanou luminozitou 30 fb^{-1}. Študovali sme metódu určenia vône B-mezónu pomocou jetov a aplikovali ju na meranie predozadnej asymetrie signálneho rozpadového módu. V závere sme porovnali niektoré vlastnosti častíc pred a po aplikovaní filtrov a diskutovali vplyv selekcie na pozorované spektrá.

Klíčová slova: ATLAS, vzácne B rozpady, B_s^0, ϕ, predozadná asymetria

Title: Study of rare B decays in ATLAS
Author: Ina Chalupková
Department: Institute of Particle and Nuclear Physics
Supervisor: doc. RNDr. Zdeněk Doležal, Dr.
Consultant: Mgr. Pavel Řezníček
Supervisor's e-mail address: dolezal@ipnp.troja.mff.cuni.cz

Abstract: In this work is studied the semileptonic rare decay $B_s^0 \to \phi^0 \mu^+ \mu^-$ in ATLAS detector at CERN. Offline analysis have been performed and selection cuts were found and optimized by comparing distributions for signal and background Monte Carlo data. The selection efficiencies and background suppression factors were computed, as well as the estimated number of detected events in data with an integrated luminosity of 30 fb^{-1}. The jet flavour tagging method was studied and applied on measurement of forward-backward asymmetry in signal decay. Spectra of particle properties before and after applying offline selection cuts were compared and the influence of cuts on measurements was discussed.

Keywords: ATLAS, rare B decays, B_s^0, ϕ, forward-backward asymmetry

Chapter 1

Introduction

Rare decays of beauty hadrons are forbidden at tree-level in the Standard Model (SM) and appear as heavily Cabibbo-suppressed Flavour Changing Neutral Currents (FCNC) in loop diagrams. These loops may contain contributions of potential new particles and provide new possibility of search for physics beyond Standard Model (BSM). Taking into account a low branching ratio of rare decays, a good trigger and event selection is needed to suppress background, which has a rate several orders of magnitude higher than the signal rate.

In the beginning of this thesis in Chapter 2 is given a brief overview of the LHC accelerator and ATLAS detector, describing its magnetic system, subdetectors and trigger with focus on B-physical trigger. Chapter 3 reviews the basic theoretical description of semileptonic rare decays in the Standard Model, discussing observables such as branching ratio or forward-backward asymmetry, which are less influenced by theoretical uncertainties and can be used in new physics searches. More into details is described the $B_s^0 \to \phi^0 \mu^+ \mu^-$ decay, its detection and possible background sources. In Chapter 4 is shortly introduced the Monte Carlo data simulation and analysis framework on ATLAS and details about signal and background datasets used for analysis are given.

The core of this work is summarized in Chapter 5 along with the results of offline analysis of $B_s^0 \to \phi^0 \mu^+ \mu^-$ decay. By comparing distributions of variables for signal and background data and considering kinematics, detector and other conditions are found event selection cuts. Their efficiencies of selection and background suppression are presented and the estimated numbers of detected events in data with integrated luminosity 30 fb^{-1} are computed. In the same chapter is described and studied the jet flavour tagging method, which is applied in the measurement of forward-backward asymmetry. Finally, particle properties after offline selection are shown and the cut influence on their measurement is discussed.

In the whole thesis the system of natural units ($\hbar = \text{c} = 1$) is used.

Chapter 2

ATLAS Experiment at LHC

2.1 The Large Hadron Collider

The Large Hadron Collider (LHC) is a superconducting particle accelerator and collider located in The European Organization for Nuclear Research (CERN) in Geneva, Switzerland. It is installed in a tunnel situated 50 to 175 meters under ground with circumference 26 659 m, previously used by the Large Electron-Positron Collider (LEP). LHC was designed to collide proton beams with center-of-mass collision energy up to 14 TeV at peak luminosity 10^{34} cm^{-2}s^{-1}. It will also accelerate and collide heavy ions (lead $^{208}\mathrm{Pb}^{82+}$) with energy up to 2.76 TeV per nucleon at nominal luminosity 10^{27} cm^{-2}s^{-1}. Beam bunches will cross every 25 ns and at design luminosity and energy there will be approximately 23 interactions per crossing [1].

Luminosity $\mathcal{L}$ is a machine parameter, for collider with two opposing beams defined as

$$\mathcal{L} = F\frac{fn_1n_2}{4\pi\sigma_x\sigma_y} \tag{2.1}$$

where F is the geometric luminosity reduction factor depending on the angle of beam crossing, f is the bunch collision frequency, n_1 and n_2 the number of particles in each bunch of beam 1 or 2 respectively and σ_x and σ_y are parameters of beam profile. The total number of events per second N, for a process with cross section σ, is than equal to

$$N = \mathcal{L}\sigma \tag{2.2}$$

At the four interaction points (IP) of LHC beams, there are installed four major experiments each one executing a dedicated physics program. Two of them are general-purpose experiments surrounding their IP almost completely, ATLAS (A Toroidal LHC ApparatuS) and CMS (Compact Muon Solenoid). The other two are the smaller LHCb (Large Hadron Collider bphysics), which is built in forward direction and has B-physics oriented scientific program, and ALICE (A Large Ion Collider Experiment) covering nearly full spatial angle around IP by asymmetrically placed subdetectors, which is primarily dedicated to study

heavy ion collisions. There are also three smaller experiments installed in order to maximize the discovery potential offered by LHC. Detectors TOTEM (TOTal Elastic and diffractive cross section Measurement) and LHCf (Large Hadron Collider forward) are specialized on forward physics and the newest MoEDAL (Monopole and Exotics Detector at the LHC) aims to search for new particles behind Standard Model (SM).

LHC is currently operating with protons at the center-of-mass energy of 7 TeV (planned for period of 2010 – 2011) with peak luminosity up to $1.6 \times 10^{30}\mathrm{cm}^{-2}\mathrm{s}^{-1}$ (at IP1, ATLAS, Ref. [2]).

2.2 ATLAS Experiment

ATLAS is one of the two general-purpose experiments at LHC [3]. Its aim is to study a wide spectrum of physical topics, among them the existence of not-yet-discovered Higgs boson, predicted by the Standard model and explaining the origin of matter in spontaneous symmetry breaking mechanism, more Higgs particles, signatures of extra spatial dimensions, black holes, gravitons, heavy particles predicted by supersymetry (SUSY) or other beyond-standard model theories. An important part of ATLAS interests are precise measurements of Standard model parameters. The fact that the cross section for heavy quarks production (b and t) is high at LHC energies makes this collider a powerful b-factory and allows CP violation effects and elements of CKM matrix to be measured, as well as t-quark properties. This program will take part especially during the initial low luminosity running [4].

In order to maximize its performance, ATLAS detector was designed as a cylindrical detector covering nearly full spatial angle around the IP. It is composed of different specialized sub-detectors, which perform measurements of particle properties and also their identification. Cross checking of the quantities measured by different detectors is important to improve understanding of signals and results interpretation.

The ATLAS layout is shown in Figure 2.1. Spatial position inside the detector can be described by the cylindrical coordinates z, R and ϕ, where the z-axis is following the beam direction and crossing the interaction point (in Point 1 positive z points to Point 8), R is radius and ϕ azimuthal angle with ϕ=0 horizontal and pointing into the center of LHC ring. If Cartesian coordinates are used, positive x-axis is horizontal pointing inside of the ring and y-axis points upwards. Polar angle θ is measured from the positive z axis. More often the pseudorapidity is used, defined as

$$\eta = -\log\left(\tan\frac{\theta}{2}\right) \tag{2.3}$$

Another important quantity, transverse momentum p_{T}, is defined as the momentum perpendicular to the LHC beam axis. Transverse energy E_{T} is defined in similar way.

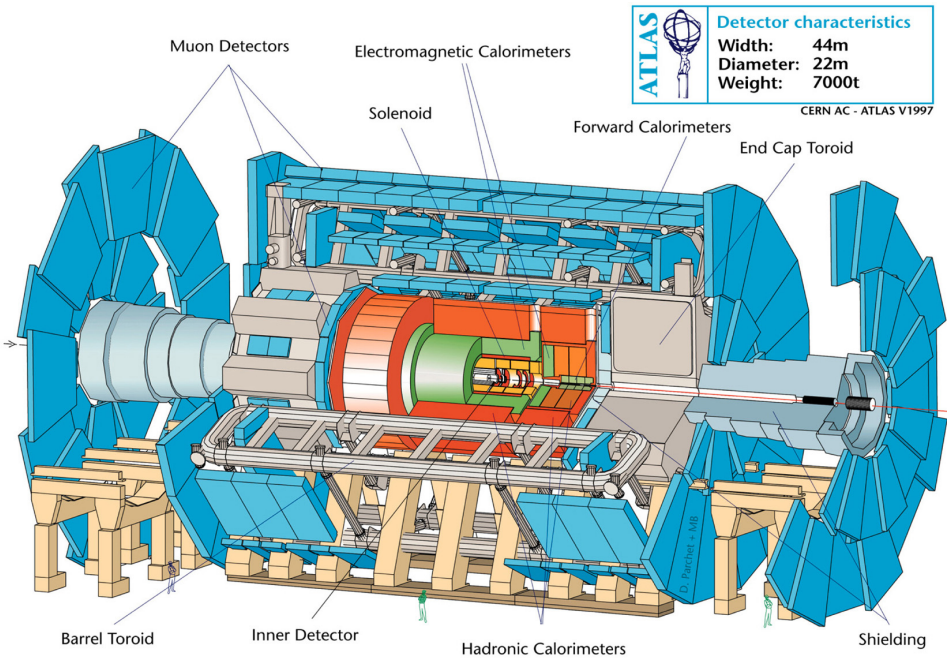

Figure 2.1: Layout of the ATLAS detector.

2.2.1 ATLAS Magnet System

The ATLAS magnet system consists of an inner superconducting solenoid and 8 large superconducting air-core toroids. The central solenoid with a length of 5.3 m and diameter of 2.4 m is positioned inside the barrel electromagnetic calorimeter and provides a magnetic field of 2 T allowing precise momentum measurements in the inner detector. Its thickness have been minimized to avoid influencing calorimeter performance.

The air-core toroid magnet system consists of 25,3 m barrel part and two end-caps with lengths 5.6 m and outer diameter of 10.7 m, inserted at each end of the barrel. Each toroid consists of eight flat coils symmetrically arranged around the beam axis. The magnetic field of toroids is not homogeneous, its peak values are 3.9 T for barrel and 4.1 T for end-caps. The toroid magnets are providing a large magnetic field with a strong bending power within a light and open structure, where the Muon Spectrometer is installed. They are bending charged-particle trajectory in η direction, while solenoid is bending it in ϕ.

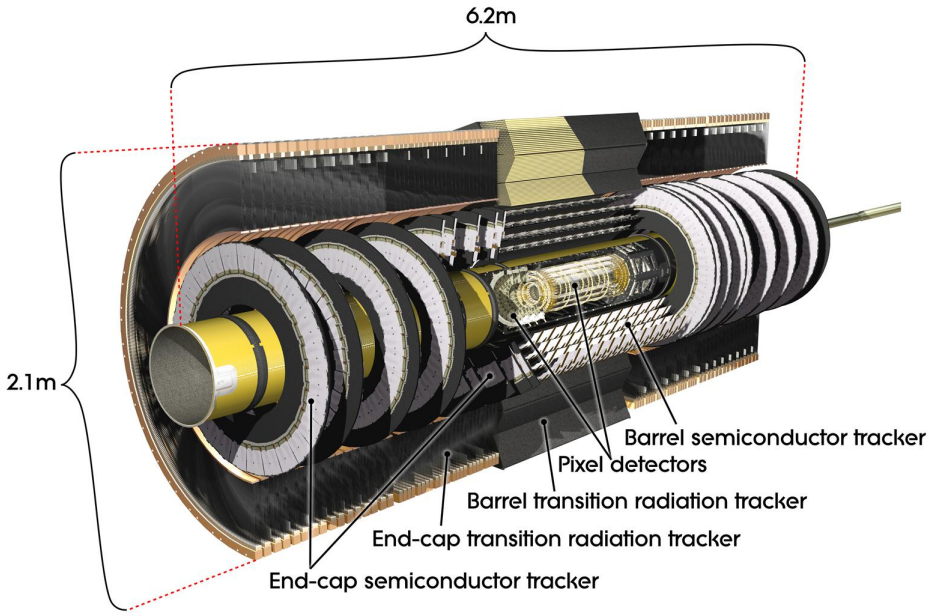

Figure 2.2: ATLAS Inner Detector [5].

2.2.2 ATLAS Subdetectors

The innermost part of ATLAS, the Inner detector, is contained in a cylinder with length 6.2 m and radius 1.15 m. A pattern recognition, accurate momentum and vertex measurements as well as electron identification are achieved with a combination of discrete high-resolution silicon pixel and strip detectors in the inner part and continuous tracking detectors with transition radiation tubes in its outer part, see Figure 2.2.

The Pixel detector is formed by three layers in the barrel region and five end-cap discs on each side, with η coverage $\pm$2,5 for barrel and 1.5 – 2.7 for end-caps. Silicon pixels are 50 µm wide in $R\phi$ direction and 400 µm long. This high granularity contributes to accurate vertex measurement.

The strip detector, SemiConductor Tracker (SCT), is made of four barrel layers (η coverage $\pm$ 1.4) and nine end-cap discs ($|\eta|$ from 1.4 to 2.5). The strips have 80 µm pitch, 12 cm length and to determine two-dimensional position on module, the two layers of strips are rotated by 40 mrad with respect to each other. SCT is adding another space points to the ones measured by Pixel and is helping to measure particle momenta more precisely. Each layer of Pixel detector and SCT consist of a number of independent detector modules (pixels or strips respectively) and read-out electronics. However, the total number of layers was limited by the need to minimize power dissipation caused by material (e.g. multiple Coulomb scattering, electron bremsstrahlung, photon conversion to electron-positron pair).

The most outer part of the Inner detector, Transition Radiation Tracker

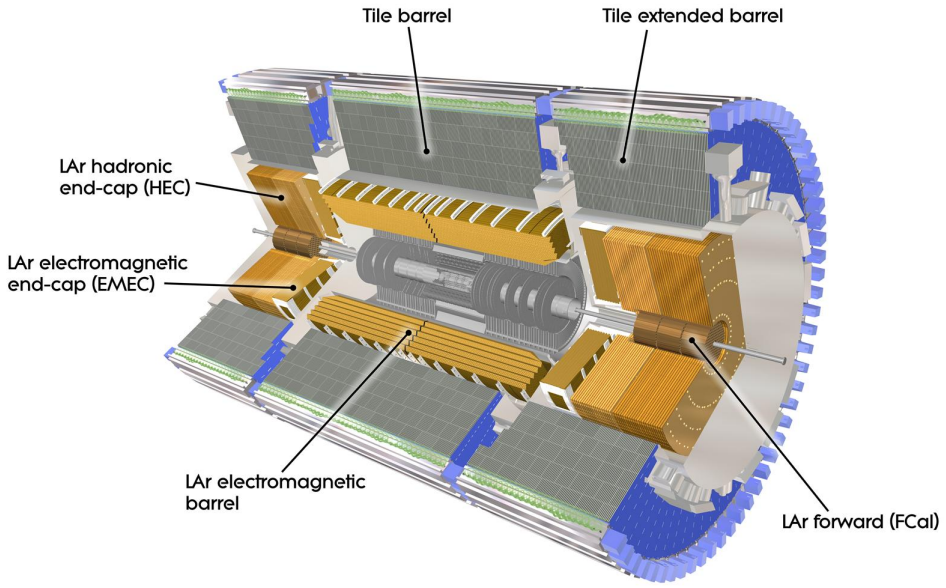

Figure 2.3: Schematic view of ATLAS calorimeter system.

(TRT), is covering η region $\pm$ 2.0 and it is composed of 4 mm diameter drift tubes, which are filled with a gas mixture. Tubes are organized into 36 layers inter-spaced with a radiator to emit transition radiation of electrons, so that the passage of charged particle is measured through the gas ionization and at the same time the transition radiation photons are absorbed by the gas molecules. There are two thresholds for recording hits used to distinguish between electrons and hadrons.

ATLAS calorimeter system schematically shown in Figure 2.3 is contained in a cylinder with a radius of 4.25 m and a width of 12.2 m. Its inner part, Electromagnetic Calorimeter (EMCal), is a high granular liquid-argon (LAr) sampling calorimeter covering pseudorapidity region $\pm$ 4.9, which measures with great accuracy the energy of the shower produced by photons, electrons and positrons. High segmentation of EMCal together with accordion-like layer structure allows one to measure the shape of electromagnetic shower developed in lead absorber plates and is essential to reject jet backgrounds and particle identification. Shower leakage behind the EM Calorimeter contributes to lower energetic resolution, that is why the EMCal was designed with a minimum depth[1] of 26 X_0 in the barrel and 28 X_0 in the end-cap.

The next detector, Hadronic calorimeter in the barrel region uses iron absorbers with scintillator plates (forming the tile structure, TileCal). Barrel is composed by one central part and two extended barrel cylinders on each side,

[1]The depth of calorimeter, i.e. the amount of material in the path of particle from IP is given in radiation length X_0, which is the scaling variable for the probability of occurrence of bremsstrahlung and pair production of electromagnetic-interacting particles in given material.

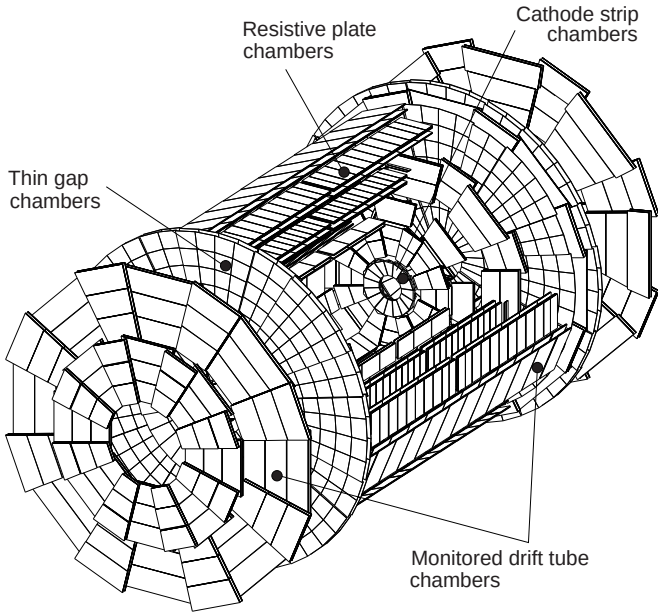

Figure 2.4: Layout of ATLAS Muon spectrometer.

together covering a total pseudorapidity of $|\eta| < 1.7$. Three longitudinal sections together with material of support structures represent the length[2] of 11 λ. The extended Tile barrel is enlarging the pseudorapidity coverage region to $\eta \pm 3.2$. Hadronic end-caps at $|\eta| = 3.1$ – 4.9 and forward calorimeters (FCal) are both using the LAr technology. The purpose of Hadronic calorimeter is to identify jets and measure their energy and direction, measure the total missing transverse energy and improve the particle identification by measuring quantities such as leakage and isolation.

Hadronic calorimeter is surrounded by superconducting air-core toroidal magnet, which provides a powerful magnetic field needed for the Muon Spectrometer precision measurements. Four types of muon detectors are used. In the barrel, resistive plate chambers (RPC) are used for the trigger and monitored drift tube chambers (MDT) for an accurate tracking. In the end-caps, thin gap chambers (TGC) are used for the trigger, MDT and cathode strip chambers (CSC) for the tracking. A layout of Muon system is shown in Figure 2.4.

The momentum measurement is based on a deflection of muon trajectories in the magnetic field of three air-core toroids, which is mostly orthogonal to the muon trajectories. The chambers are arranged in three super-layers called *stations* along the muon trajectory. In the barrel, the three detector stations (each made of six or eight layers of MDT) are placed concentrically around the beam line in radial distance 5 m, 7.5 m and 10 m, and they cover a pseudorapidity of $|\eta| < 1$.

[2]The thickness in interaction length λ defined for hadrons in a similar way as radiation length of electrons and photons.

Momentum is determined using sagitta[3] of muon track. In the end-cap regions, the MDT chambers are arranged in four discs orthogonal to the beam axis placed at distances of 7, 10, 14 and 22 m from IP. At a large pseudorapidity, close to the beam axis, CSC chambers with high radiation hardness are used. Due to the fact that magnetic field is present just between inner and middle station momentum is determined by the so called *point-angle* measurement, using a point in the inner station and the angle between hits in middle and outer station.

The muon trigger system is based on fast momentum measurement using a track vector and known nominal interaction point. In order to accommodate both triggering capability at low p_{T} (to maximize rates for B-physics) and high threshold for high luminosities, trigger detectors are placed in three stations in barrel region. The first two layers of RPC are on both sides of the middle MDT station providing low p_{T} threshold (4 of 6 GeV), with third station added to outer precision chamber with a typical threshold of 20 GeV. A similar concept is used in end-cap regions, where TGC chambers are placed near the middle station. The muon trigger system covers a pseudorapidity range of $|\eta| < 2.4$.

2.2.3 Trigger System

Bunches of LHC will cross every 25 ns leading to an event rate of 40 MHz, and about 23 inelastic proton-proton collisions will be delivered every crossing (at design luminosity). As the average data size is 1.5 MB per event, this would produce a data flow too high for currently available data storage technology. The major part of data are representing minimum bias events with low interest, so there is no need to save them. That is why a complex hardware and software system called *trigger system* was designed to select interesting events and suppress their background at the same time. Its another important role is to assign data to correct bunch crossing (note that high-energy muon time of flight from IP to muon chambers is comparable to the time between two bunch crossings). The ATLAS strategy is to use inclusive trigger algorithms as much as possible to maximize possible physics coverage and to be open to new signatures.

ATLAS trigger is based on three levels: Level-1 (LVL1), Level-2 (LVL2) and Event Filter (EF) [6]. LVL2 and EF are known also under a name High-Level Trigger (HLT). The LVL1 trigger will make the first level of event selection, reducing initial event rate to less than 75 kHz. Operation at up to about 100 kHz is possible with increased dead-time. The HLT must reduce the event rate to around 100 Hz. In Figure 2.5 are shown the processing times available for each trigger level together with the output rates.

LVL1 trigger is a fast hardware based system analyzing data from calorimeters and muon system with latency around 2 µs. Both calorimeters are read out with low granularity and muons from RPC and TGC chambers with p_{T} higher than threshold are reconstructed ($p_{\mathrm{T}} \geq 4$ or 6 GeV), while data from other subdetectors

[3]Sagitta is a distance of middle space point from straight line connecting points measured by inner and outer station.

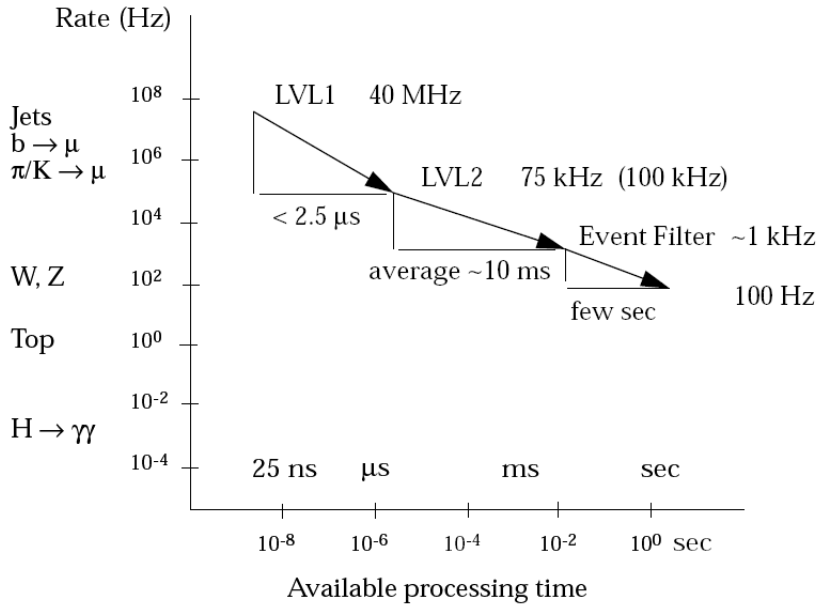

Figure 2.5: Processing times and output rates of ATLAS trigger subsystems [4]

are stored in pipeline memories waiting for LVL1 decision and than moved to Read-out Buffers (ROB) accessible by LVL2. LVL1 is using simple algorithms to create objects called *regions of interest* (RoI), that are containing its position and information about the threshold they passed. For muon RoI they include p_{T} threshold, while for EM/Tau RoI isolation of electromagnetic shower is included. Candidates for EM/Tau RoI, photon and electron, are not distinguishable in EMCal, τ-leptons are identified by evidence of jets produced in both EMCal and TileCal, and Jet RoI has given minimal E_{T} deposited in TileCal. Values of total and missing E_{T} are stored as well.

Next trigger level, LVL2 should reduce data to rate around 1 kHz with processing time varying from 1 μs to 10 μs according to event complexity. It is using output from LVL1 and part of data from all detectors (stored in ROB's) that was flagged as RoI's. Data are analyzed, so called *features* (trigger objects on detector level, such as tracks or calorimeter clusters) are formed and combined into physics objects candidates (electrons, photons, jets, etc.). These objects are processed by hypothesis algorithms, which perform fast analysis of physics process, for example assigning more particle candidates to a primary particle and applying cuts on its invariant mass or lifetime. If an event is accepted, its data are written into the Full Event Buffers.

Final reduction of the event rate to values around 100 Hz is performed by EF layer of ATLAS trigger with processing time up to 1 s. It has already access to full data from subdetectors, however it is still guided by information about physics object candidates from the previous level. Data are analyzed using complex algorithms with high performance in tracking, vertexing and computation of

physical quantities.

During initial data-taking Minimum Bias Trigger Scintillators (MBTS) are used to study minimum bias events at low luminosity. MBTS are forming two rounds mounted at each end of the detector in front of the LAr end-caps and read out by TileCal. Two independent triggers were developed, one uses trigger scintillator signals at LVL1 and possibly further processing on HLT. The alternative approach is using a random trigger at LVL1 and performing a track based selection on HLT. After 3–4 months of higher luminosity will the operation of MBTS end due to the radiation damage.

2.2.4 B-physics Trigger

At design LHC energy in about 1% of collisions will be produced $b\bar{b}$ pairs. As every field of study, also B-physics will have just limited trigger resources available, therefor B-trigger should select interesting events with good efficiency and the highest possible background rejection. Taking into account dynamics and detector signatures of B-hadron decays in ATLAS physic program (will be described in section 3.2), B-trigger is based on the detection of di-muonic final states.

Search for muon pairs can be done in two ways: by using di-muon trigger with LVL1 muons confirmed in the HLT, what provides a trigger for $B \to \mu\mu$ and $B \to \mu\mu X$, as well as for decays with $J/\psi\,(\mu\mu)$ in the final state. Second possible setup is to use single LVL1 muon in conjunction with a second muon found at LVL2 inside the same RoI (trigger for $J/\psi \to \mu\mu$ with the momentum of the second muon below the LVL1 threshold), track reconstructed inside a Jet RoI (hadronic final states) or EM RoI (not implemented yet, electron confirmed by HLT would be useful for $J/\psi \to ee$ selection, photon for radiative decays such as $B \to \phi\gamma$).

The first trigger, hardware-based LVL1 muon trigger is using fast muon chambers (RPC and TGC) and its schematic view in Rz plane is shown in Figure 2.6. A hit in one of the stations called *pivot plane* (in schema labeled as RPC1 and TGC3) is extrapolated along a straight line from IP through other two stations, where is expected a hit in $\eta \times \phi$ window around their intersection point. The size of the window is depending on p_{T} threshold. The plane closer to the pivot plane is used for low p_{T} cut and the further one for high p_{T}.

LVL2 muon trigger first confirms LVL1 muon(s) by precision chambers allowing more precise momentum measurement. Tracks are than extrapolated to the calorimeter and Inner detector. By matching tracks the main background for LVL1 muons from K/π decays can be suppressed in this phase. One type of di-muon trigger requires two RoI's from LVL1 confirmed at LVL2. The second algorithm is extending one LVL1 RoI and searching for the second muon by track in Inner detector. This is allowing to accept also muon with lower p_{T} than threshold, but on the other hand the reconstruction of a larger region is much slower and a higher fraction of background events is passing this trigger. At initial LHC luminosity di-muon and single muon LVL1 trigger will be used, followed

by partial B-decays reconstruction at LVL2. With higher luminosity the di-muon trigger will be used and reconstruction at LVL2 will be done only in RoI's [7].

The EF is than guided by LVL2 results and performs more precise muon and hadron track reconstruction, vertexing and mass cuts (with nearly offline quality).

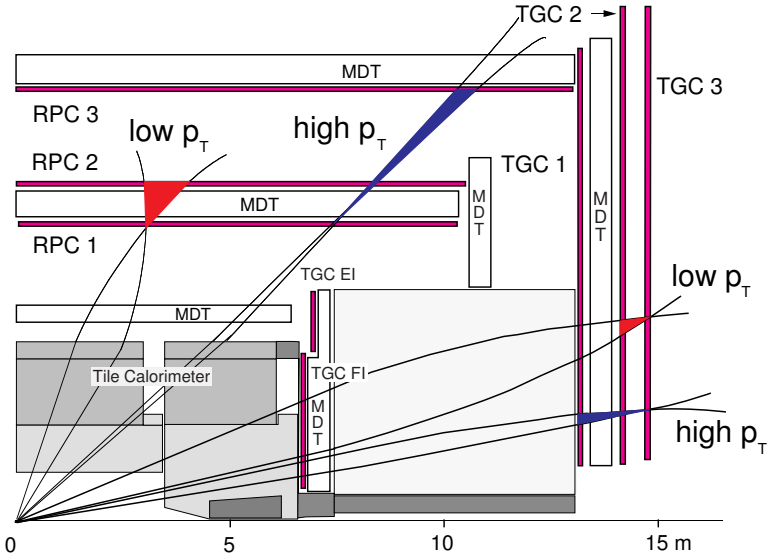

Figure 2.6: Schema of LVL1 muon trigger.

Chapter 3

Semileptonic Rare Decays of Beauty Hadrons

By rare B decays, one usually understands heavily Cabibbo-suppressed quark transitions $b \to u$ or Flavour Changing Neutral Currents (FCNC) $b \to s$ or $b \to d$ that in the Standard Model (SM) are forbidden at tree-level, hence they have small branching ratios in the order of 10^{-5} or smaller. In SM these decays can occur only through loops, which contain contributions of potential new particles, and provide a valuable possibility of an indirect search of physics beyond SM and offer a complementary strategy to direct searches of these particles. In addition, if assuming the validity of SM, rare FCNC decays allow the measurement of the CKM matrix elements $|V_{ts}|$ and $|V_{td}|$ and thus complement their determination from B^0–$\bar{B}^0$ or B_s^0–$\bar{B}_s^0$ mixing.

There are three types of rare B decays: purely leptonic, radiative and semileptonic. Purely leptonic decays are represented for example by the decay $B^0 \to \mu^+\mu^-$ with only muons in final state. The second, radiative decays have photon in the final state like for instance exclusive decay $B \to K^*(892)\gamma$ or inclusive $B \to X_s\gamma$. In this thesis we focus on the third type, semileptonic rare B decays with both hadrons and leptons in final state, in particular the decay $B_s^0 \to \phi^0\mu^+\mu^-$.

3.1 Theoretical Framework

At quark-level, $b \to q\ell^+\ell^-$, $q = (d, s)$, transitions arise form W/t-penguin or W-box Feynman diagrams shown in Figure 3.1. Interaction is described in terms of an effective Hamiltonian obtained by integrating out virtual effects of heavy particles (top quark, W and Z bosons in the SM) [8]:

$$\mathcal{H}_{\text{eff}}^q = -\frac{4G_F}{\sqrt{2}} V_{tb}V_{tq}^* \sum_{i=1}^{11} C_i(\mu)\mathcal{O}_i^q(\mu), \tag{3.1}$$

where G_F is the universal Fermi constant, V_{tb} and V_{tq}^* are elements of CKM matrix with $q = s, d$ and $\mathcal{O}_i^q$ are local renormalized operators. $C_i(\mu)$ are Wilson

coefficients, which can be calculated in perturbation theory and encode the relevant short-distance physics, in particular any potential new-physics effects. The renormalization-scale μ can be viewed as separating the long- and short-distance regimes and its value has to be chosen as $\mu \sim m_b$ for calculating decay rates from Eqn. (3.1). However, the operator basis used here is not complete for some models. For instance in those exhibiting left-right symmetry, new physics also shows up in the form of new operators.

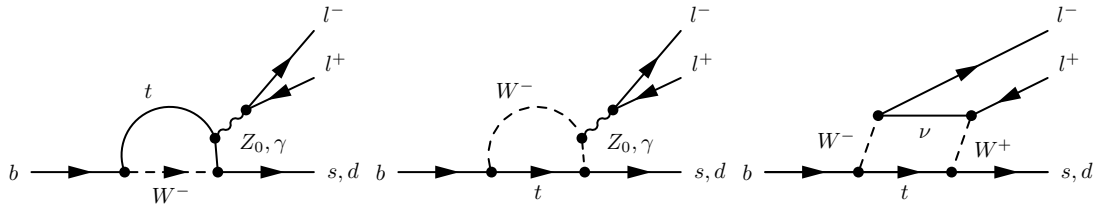

Figure 3.1: t-penguin (left), W-penguin (middle) and box (right) Feynman diagrams for the electroweak decay $b \to (s,d)\ell^+\ell^-$.

On the other hand, taking into account quark confinement in hadrons, long-distance effects will also influence observed values. For semileptonic rare decays can be the effective Hamiltonian of $b \to s\ell^+\ell^-$ formulated as (at free quark level, see [9] for details)

$$\mathcal{H}^s_{\rm eff} = \frac{G_F \alpha \lambda_t}{\sqrt{2}\pi} \left[C_8^{eff}(\mu) \bar{s}_L \gamma_\mu b_L \bar{\ell} \gamma^\mu \ell + C_9 \bar{s}_L \gamma_\mu b_L \bar{\ell} \gamma^\mu \gamma_5 \ell - \frac{2 m_b C_7(\mu)}{q^2} \bar{s}_L i \sigma_{\mu\nu} q^\nu b_R \; \bar{\ell} \gamma^\mu \ell \right], \tag{3.2}$$

where $x_t \equiv m_t^2/m_W^2$, $\lambda_t = V_{ts}^* V_{tb}$, and $C_8(\mu)$, C_9 and $C_7(\mu)$ are Wilson coefficients.

We parametrize the transition matrix elements of $B_s \to \phi\ell^+\ell^-$ in terms of the relevant form factors as follows:

$$\begin{aligned}
\langle \phi(p_2,\epsilon)| \; V_\mu \mp A_\mu \; |B_s(p_1)\rangle &= \frac{1}{m_{B_s} + m_\phi} \Big[-iV(q^2) \varepsilon_{\mu\nu\alpha\beta} \epsilon^{*\nu} P^\alpha q^\beta \\
&\quad \pm A_0(q^2) \, (P \cdot q) \, \epsilon_\mu^* \pm A_+(q^2) (\epsilon^* \cdot p_1) P_\mu \\
&\quad \pm A_-(q^2) (\epsilon^* \cdot p_1) q_\mu \Big] \, , \\
\Big\langle \phi(p_2,\epsilon)| \; (T_{\mu\nu} \pm T^5_{\mu\nu}) q^\nu \; |B_s(p_1)\Big\rangle &= -ig(q^2) \varepsilon_{\mu\nu\alpha\beta} \epsilon^{*\nu} P^\alpha q^\beta \\
&\quad \pm a_0(q^2) \, (P \cdot q) \left[\epsilon_\mu^* - \frac{1}{q^2} \, (\epsilon^* \cdot q) \, q_\mu \right] \\
&\quad \pm a_+(q^2) (\epsilon^* \cdot p_1) \left[P_\mu - \frac{1}{q^2} \, (P \cdot p_1) \, q_\mu \right]
\end{aligned} \tag{3.3}$$

where m_{B_s} and m_ϕ are the meson masses, $p_1(p_2)$ is the momentum of the initial (final) meson, ϵ is the polarization vector of ϕ meson, $P = p_1 + p_2$, $q = p_1 - p_2$, $V_\mu = \bar{q}_2 \gamma_\mu q_1$, $A_\mu = \bar{q}_2 \gamma_\mu \gamma_5 q_1$, $T_{\mu\nu} = \bar{q}_2 i \sigma_{\mu\nu} q_1$, $T^5_{\mu\nu} = \bar{q}_2 i \sigma_{\mu\nu} \gamma_5 q_1$, and V, $A_{0,\pm}$, g,

and $a_{0,\pm}$ are the form factors. Since these calculations are in non-perturbative theory, phenomenological quark models may be useful. Taking into account that in energetically accessible region $0 \leq q^2 \leq (m_{B_s} - m_\phi)^2$ ϕ-meson may become highly relativistic, the approach of *Light Front Quark Model* (LFQM) is often used. In LFQM can be done a consistent and fully relativistic treatment of quark spins and the center-of-mass motion. More detailed explanation, parametrization and application of LFQM to meson decay computations can be found for example in Ref. [9] or more detailed description in [10].

3.1.1 Decay Amplitudes and Decay Rates

Using equations (3.2) and (3.3) in LFQM framework we obtain decay amplitudes of $B_s \to \phi\ell\bar{\ell}$ as follows:

$$\begin{aligned}\mathcal{M}(B_s \to \phi\ell^+\ell^-) = \frac{G_F\alpha_{em}\lambda_t}{2\sqrt{2}\pi}\frac{2}{m_{B_s}} \\ \times\Bigg\{ \Bigg[- i\ G_V\ \varepsilon_{\mu\nu\alpha\beta}\ \epsilon^{*\nu}P^\alpha q^\beta + G_A^0\,(P\cdot q)\,\epsilon_\mu^* + G_A^+\,(\epsilon^*\cdot P)\,P_\mu \Bigg]\ \bar{\ell}\gamma^\mu\ell \\ + \Bigg[- i\ F_V\ \varepsilon_{\mu\nu\alpha\beta}\ \epsilon^{*\nu}P^\alpha q^\beta + F_A^0\,(P\cdot q)\,\epsilon_\mu^* \\ + F_A^+\,(\epsilon^*\cdot P)\,P_\mu + F_A^-\,(\epsilon^*\cdot P)\,q_\mu \Bigg]\ \bar{\ell}\gamma^\mu\gamma_5\ell \Bigg\},\end{aligned} \tag{3.4}$$

the functions $G_V,\ F_V,\ G_A^0,\ F_A^0,\ G_A^+,\ F_A^+$, and F_A^- are defined by

$$\begin{aligned} G_V &= \frac{C_8^{eff}\ V}{2(1+\sqrt{r_\phi})} - \frac{C_7\hat{m}_b g}{s}, \quad F_V = \frac{C_9\ V}{2(1+\sqrt{r_\phi})}, \\ G_A^0 &= \frac{C_8^{eff}\ A_0}{2(1+\sqrt{r_\phi})} - \frac{C_7\hat{m}_b a_0}{s}, \quad F_A^0 = \frac{C_9\ A_0}{2(1+\sqrt{r_\phi})}, \\ G_A^+ &= \frac{C_8^{eff}\ A_+}{2(1+\sqrt{r_\phi})} - \frac{C_7\hat{m}_b a_+}{s}, \quad F_A^+ = \frac{C_9\ A_+}{2(1+\sqrt{r_\phi})}, \\ F_A^- &= \frac{C_9\ A_-}{2(1+\sqrt{r_\phi})}, \end{aligned} \tag{3.5}$$

with $s = q^2/m_{B_s}^2$, $\hat{m}_b = m_b/m_{B_s}$ and $r_\phi = m_\phi^2/m_{B_s}^2$.

From Eqs. (3.2) and (3.4) the differential decay rates for $B_s \to \phi\ell^+\ell^-$ are found to be

$$\frac{d\Gamma\,(B_s \to M_s\ell^+\ell^-)}{ds} = \frac{G_F^2|\lambda_t|^2 m_{B_s}^5\alpha_{em}^2}{3\cdot 2^9\pi^5}\ (1-\frac{4t}{s})^{\frac{1}{2}}\ \varphi_{M_s}^{1/2}\left[\left(1+\frac{2t}{s}\right)\alpha_{M_s} + t\delta_{M_s}\right] \tag{3.6}$$

where

$$t = m_l^2/m_{B_s}^2, r_{M_s} = m_{M_s}^2/m_{B_s}^2, \varphi_{M_s} = (1-r_{M_s})^2 - 2s\,(1+r_{M_s}) + s^2\ . \tag{3.7}$$

The coefficients α_ϕ and δ_ϕ are given by

$$\begin{aligned}
\alpha_\phi &= 4s\left[3(1-r_\phi)^2(|G_A^0|^2+|F_A^0|^2)+2\varphi_\phi(|G_V|^2+|F_V|^2)\right] \\
&\quad +\frac{\varphi_\phi}{r_\phi}\left[(1-r_\phi)^2(|G_A^0|^2+|F_A^0|^2)+\varphi_\phi(|G_A^+|^2+|F_A^+|^2)\right. \\
&\quad \left.+2(1-r_\phi)(1-r_\phi-s)Re(G_A^0G_A^{+*}+F_A^0F_A^{+*})\right] \qquad (3.8)\\
\delta_\phi &= -48\varphi_\phi|F_V|^2-72(1-r_\phi)^2|F_A^0|^2+\frac{6\left[2(1+r_\phi)-s\right]}{r_\phi}\varphi_\phi|F_A^+|^2 \\
&\quad +\frac{6s}{r_\phi}\varphi_\phi|F_A^-|^2+\frac{12(1-r_\phi)}{r_\phi}\varphi_\phi Re(F_A^0F_A^{+*}+F_A^0F_A^{-*}+F_A^+F_A^{-*})\ .
\end{aligned}$$

Decay rate for the $B_s \to \phi\mu^+\mu^-$, neglecting the interference effects with the much stronger $B_s \to \phi\, J/\psi$ and $B_s \to \phi\ \psi(2S)$ decays, is predicted to be $\mathcal{B} = 1.64 \times 10^{-6}$ (see Ref. [9]).

Many systematic uncertainties cancel in measurement of the relative branching ratio

$$\frac{\mathcal{B}(B\to\mu^+\mu^-\phi)}{\mathcal{B}(B\to J/\psi\ \phi)} = \frac{N_{\mu^+\mu^-\phi}}{N_{J/\psi\phi}}\frac{\varepsilon_{J/\psi\phi}}{\varepsilon_{\mu^+\mu^-\phi}} \times \mathcal{B}(J/\psi\to\mu^+\mu^-), \qquad (3.9)$$

where $N_{\mu^+\mu^-\phi}$ is the observed number of $B \to \mu^+\mu^-\phi$ decays, $N_{J/\psi\phi}$ is the number of $B \to J/\psi\ \phi$ events (called normalization decay), while $\varepsilon_{\mu^+\mu^-\phi}$ and $\varepsilon_{J/\psi\phi}$ are the combined selection efficiencies and acceptances of the experiment for $B \to \mu^+\mu^-\phi$ and $B \to J/\psi\ \phi$ respectively. Values of efficiencies can be evaluated from Monte Carlo studies of detector and event selection, often is given also the relative acceptance defined as

$$A_{\rm rel} = \frac{\varepsilon_{J/\psi\phi}}{\varepsilon_{\mu^+\mu^-\phi}}\ . \qquad (3.10)$$

3.1.2 Forward-Backward Asymmetry

Problematic hadronic form-factor uncertainties entering calculations above are the reason to introduce observables that are less affected by the uncertainties and are therefore a better basis for BSM searches. The most frequently used forward-backward asymmetry $\mathcal{A}_{\rm FB}$ is defined through the angle θ between the μ^+ and the B-hadron momenta in di-muon centre-of-mass system as

$$\mathcal{A}_{\rm FB}(s) = \frac{1}{d\Gamma/ds}\left(\int_0^1 d(\cos\theta)\frac{d^2\Gamma}{ds\,d\cos\theta} - \int_{-1}^0 d(\cos\theta)\frac{d^2\Gamma}{ds\,d\cos\theta}\right) \qquad (3.11)$$

In the SM using formalism introduced above we get

$$\mathcal{A}_{\rm FB} = \frac{12s\varphi_\phi^{\frac{1}{2}}\left(1-\frac{4t}{s}\right)^{\frac{1}{2}}(1-r_\phi)\ Re(G_VF_A^{0*}+G_A^0F_V^*)}{(1+\frac{2t}{s})\ \alpha_\phi + t\ \delta_\phi}\,. \qquad (3.12)$$

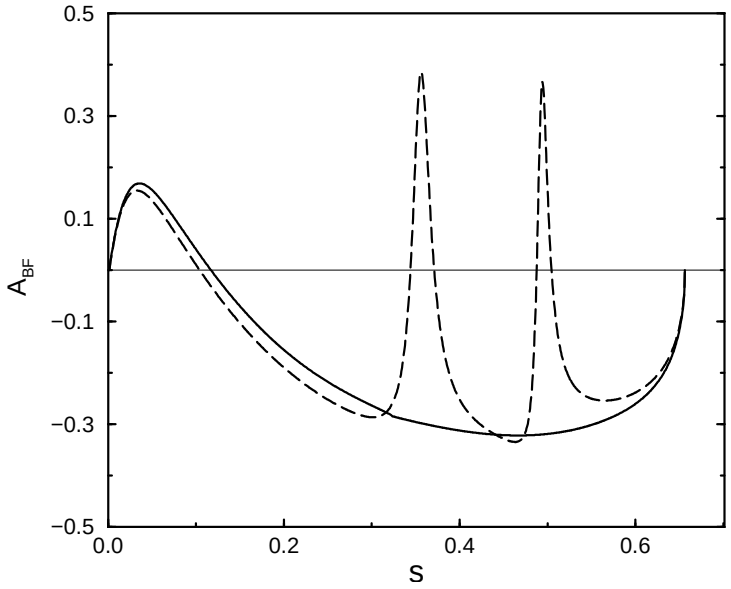

Figure 3.2: Forward-backward asymmetries in the LFQM for $B_s \to \phi\mu^+\mu^-$ as a function of $s = q^2/m^2_{B_S}$. The dashed (solid) curves represent including (non-including) long distance contributions (taken from [9]).

In Figure 3.2 is shown an example of differential $\mathcal{A}_{\rm FB}$ as a function of $s = q^2/m^2_{B_S}$ as computed in [9]. $\mathcal{A}_{\rm FB}(B_s \to \phi\mu^+\mu^-)$ is changing sign at $s = s_0 \simeq 0.1$, what is another useful observable. The value of s_0 depends on Wilson coefficients and it is insensitive to the hadronic form-factor uncertainties.

3.2 Semileptonic Rare B Decays at ATLAS

ATLAS has a dedicated B-Physics program which concentrates on measurements that extend the discovery potential for physics beyond the SM. In the sector of rare B-decays ATLAS concentrates on the decays with two muons in final state. Other channels cannot be triggered with reasonably high efficiency due to detector and trigger design. In the family of semi-muonic rare decays, ATLAS prepares measurements in six decay channels of hadrons B^0_d, B^0_s, Λ_b (see Ref. [7]):

- $B^+ \to K^+\mu^+\mu^-$
- $B^0_s \to \phi^0\mu^+\mu^-$ followed by $\phi^0 \to K^+K^-$
- $B^0_d \to K^{*0}\mu^+\mu^-$, $K^{*0} \to K^+\pi^-$
- $\Lambda_b \to \Lambda^0\mu^+\mu^-$, $\Lambda^0 \to p^+\pi^-$
- $B^+ \to K^{*+}\mu^+\mu^-$ with $K^{*+} \to K^0_S\pi^+$ and $K^0_S \to \pi\pi$

- very rare [1] decays $B^0_{d,s} \to \mu^+\mu^-$

Thanks to precise muon system extended over a large solid angle with good efficiency (90% for 6 GeV muons [6]) in combination with Inner detector with good mass resolution, particle identification and vertexing, ATLAS can provide measurements of final states of these processes with high resolution. Interesting observables are especially forward-backward asymmetry defined above, branching ratios or di-muon mass spectrum.

3.2.1 Decay $B^0_s \to \phi^0\mu^+\mu^-$

The signature of $B_s \to \phi\mu\mu$ events is the presence of the muon pair with opposite charges. Due to long B_s lifetime, this di-muon pair is usually originating from a secondary vertex detached from the primary vertex. The identification of B_s decay vertex close to the interaction point requires leptons which are well reconstructed.

Another decay product, the ϕ meson has large decay width $\Gamma = 4.26$ MeV [11], therefore it will decay practically in the B_s decay vertex. For detection was chosen a pair of K^+K^- mesons with branching ratio $\mathcal{B}(\phi \to K^+K^-) = 48.9\%$.

The event selection is done in the following order:

- primary vertex reconstruction, if more than one primary vertex has been reconstructed in the event, the one with the highest number of associated tracks is chosen
- muon and di-muon selection
- kaons reconstruction and selection
- ϕ reconstruction (with mass inside 3σ window around PDG value)
- B_s reconstruction and selection, again inside 3σ mass window and additional requirement of momentum pointing to the primary vertex

3.2.2 Background Sources

Potential background of $B^0_s \to \phi^0\mu^+\mu^-$ decay are all events containing two oppositely charged muons and two hadrons h (h represents K or π misidentified as kaon) in the final state, especially other decays of B-hadrons due to the same p_{T} and impact parameter distributions as signal canal. The main background are these decays:

- B-hadron decay into two hadrons and $c\bar{c}$ resonance (most often J/ψ or $\psi(2S)$), followed by $\psi \to \mu\mu$. These decays have the same topology as signal decay, but fixed di-muon mass and larger branching ratios (e.g.

[1] $B^0_{d,s} \to \mu^+\mu^-$ has branching ratio $\mathcal{B} \sim 10^{-9}$, while rare B-decays have $\mathcal{B} \sim 10^{-6}$.

$\mathcal{B}(B_s \rightarrow \phi J/\psi) = 1.3 \times 10^{-3}$, approximately 100 times higher). Cut on di-muon mass can remove this background, however radiative decays of resonances to $\gamma\mu\mu$ can move outside of resonance mass window and pass selection.

- semileptonic decay chain $b \rightarrow \mu^- \bar{\nu} c$, $c \rightarrow \mu^+ \nu d\,(s)$ (with branching ratio around 1%) is most dangerous if missing mass taken by neutrinos is small. These decays can be suppressed by cut on B_s mass and tight cut on B_s momentum pointing into the primary vertex (because of missing p_{T} carried by neutrinos).

- combinatorial background from semileptonic decays of both b and $\bar{b}$ created in collision (branching ratio of $\mathcal{B}(b \rightarrow \mu\nu X) \sim 1\%$), as well as from $b\bar{b}b\bar{b}, c\bar{c}b\bar{b} \rightarrow \mu\mu X$. These muons are with high probability not originating from the same secondary vertex therefore the quality of di-muon and B_s vertex χ^2 is higher than for signal decay.

- $\mu^+\mu^-$ pair produced by Drell-Yang mechanism in combination with π/K mesons. This background can be suppressed by cuts on ϕ and B_s masses and distance of B_s vertex from IP (Drell-Yang muons are produced directly in interaction point).

- production of B_s^* with dominant decay to $B_s\gamma$ may (if γ is not detected) influence the measurement of relative branching ratio (3.9). The difference of masses $(m_{B_S^*} - m_{B_S}) \sim 49$ MeV is too low to exclude this decay from background, so B_s-mesons produced like this and decaying to the signal channel have to be taken into account in the analysis. Higher excitations as $B_{s1}(5830)$ are already out from 3σ mass window.

3.2.3 Experimental Results from Other Experiments

Large samples of B_s^0 mesons are available at experiments on Tevatron (Fermilab, USA). CDF detector measured signal peak with significance 6σ and branching ratio of $\mathcal{B}(B_s^0 \rightarrow \mu^+\mu^-\phi) = (1.44 \pm 0.33(\mathrm{stat.}) \pm 0.46(\mathrm{syst.})) \times 10^{-6}$ [12], what is well consistent with SM predictions. D0, the second experiment on Tevatron observed no events in the signal region, what is corresponding with upper limit on branching ratio of $\mathcal{B}(B_s^0 \rightarrow \mu^+\mu^-\phi) < 4.1 \times 10^{-6}$ at 95% CL [13].

Existing measurements at B-factories (Belle at KEK, BaBar at SLAC) suffer from low statistics for this decay, therefore they gave just upper limits on the branching ratio or inclusive branching ratio $\mathcal{B}(B_s^0 \rightarrow \mu^+\mu^- X)$.

Chapter 4

Monte Carlo Data Simulation

For studies in this thesis Monte Carlo (MC) data samples were used. The MC simulation in high energy physics has tree main steps:

- generation: processes in collision and particles in final state are generated using MC generator based on physics theories and phenomenology, the output of the simulation are momenta and directions of the stable particles
- simulation and digitization: final-state particles are transported through the detector according to the laws of the passage of particles through the matter and their interactions with sensitive elements of detector are converted to information in the same format as output from real detector
- reconstruction: data are reconstructed using the same algorithms as real data

Our samples were created in MC08[1] production cycle using the package *EvtGen* and generator called *PythiaB*, which is an interface to *Pythia6* developed for B-physics (rare B-decays are not included in Pythia by default) [14], [15].

For simulation of particle passage through the detector *Geant4* was used (see [16] fore details). Geant propagates particles throung detector in magnetic field, simulating scattering, energy losses and secondary particle production (showers, δ electrons). During digitalization process the information about the deposited energy is translated into the detector response. The data after this step look like data from real detector with one difference, in MC data is being saved also information about physics process and particle properties from simulation called *MC truth*. This is very useful for performance studies of analysis.

[1]Data from production MC08 were simulated with center-of-mass energy 10 GeV using some of older tools, less precise geometry, etc. However, there are no newer datasets with rare B-decays available and comparing old signal data with new background simulation at center-of-mass energy 7 GeV (already simulated) would not give correct results e.g. because of different mass and p_{T} spectra. The possible method is to perform analysis with the same center-of-mass energy 10 TeV for signal and background and try to estimate the influence of energy decrease to 7 TeV. The most significant difference will be in number of expected events due to lower cross section of $b\bar{b}$ production.

Reconstruction is performed using the same algorithms as for real data. The output of the reconstruction are physical objects such as particles, tracks, jets and computed quantities (missing p_{T}, tagged jet parameters). The difference is that in MC samples all events are reconstructed and the information about trigger decision is saved and events that have not passed trigger decision are not excluded as in real data (available just if passed trigger selection). The trigger efficiency and its dependence on kinematic variables can be than studied. One of previous results relevant for rare B-decays is shown in Figure 4.1. It is an example of trigger efficiency as a function of muon p_{T} and it is easy to see why cuts on $p_{\mathrm{T}} > 4$ GeV and 6 GeV are often used. Also trigger algorithms were applied during the reconstruction and the dependence of trigger decisions on kinematic variables can be studied.

The official software framework for simulation, digitalization and reconstruction at ATLAS is ATHENA (ATlas realization of a High Energy and Nuclear physics data analysis Architecture) ([17]). It is a flexible object-oriented C++ based framework with a large flexibility, allowing to write analysis codes detaching user from the typical implementation details. Each component (a block of software, class) has a well specified interface and functionality. An ATHENA job is configured by so-called *jobOption* files that are written in the Python scripting language and define which modules have to be executed and their parameters. AHTENA is also used in the ATLAS trigger system.

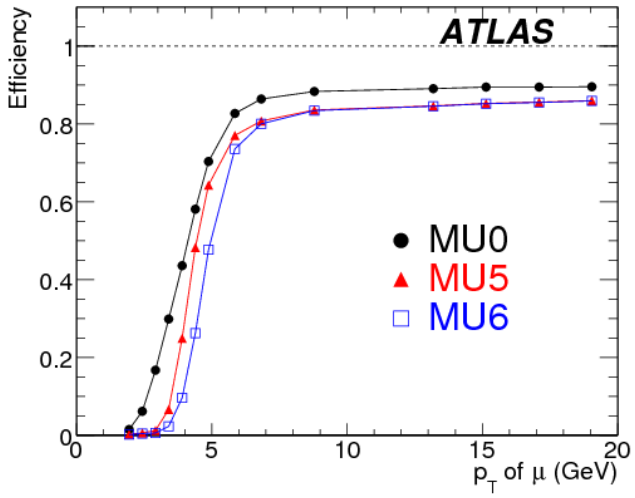

Figure 4.1: Trigger efficiency as a function of p_{T}: MU0 (filled circles), MU5 (filled triangles) and MU6 (open squares) for muons with $|\eta| < 2.5$ at the interaction point, the number in trigger name means p_{T} threshold. Taken from [5].

4.1 Signal and Background Data Samples

Data for offline analysis were in the Event Summary Data (ESD) format which contains the output of the detector simulation, digitalization and reconstruction and is produced from the raw data. It contains sufficient information for particle identification, tracking, etc. and allows performance studies of reconstruction algorithms and calibration.

In order to save computing resources, during reconstruction are often applied pre-selection cuts (in PythiaB). Samples containing di-muons were therefore generated with the requirement of both muon momenta $p_{\mathrm{T}} > 4$ GeV (*mu4mu4* in the file name) or one muon with $p_{\mathrm{T}} > 4$ GeV and the other 6 GeV (*mu6mu4*). Other cuts applied on physical quantities are listed in Table 4.1 (except of them default cuts on quark properties were included, details can be found in PythiaB configuration files for each dataset). Values of di-muon invariant mass m_{inv} are respecting decay kinematics, mass widths Γ of B_s and ϕ are wide enough not to influence subsequent offline analysis.

Quantity	Cut before vertexing	Cut after vertexing
di-muon m_{inv}	< 9 GeV	< 8 GeV
Γ_{B_S}	3 GeV	2 GeV
Γ_{ϕ}	0.3 GeV	0.25 GeV

Table 4.1: Pre-cuts applied on quantities in MC event generation.

In this thesis are analyzed fully reconstructed samples listed in Table 4.2. In the following text the tag will be sometimes used instead of dataset number or process (in plots or in case of subscripts such as σ_{sig}, σ_{bb}), when mentioning the signal decay/channel, $B_s \to \phi\mu^+\mu^-$ decay followed by $\phi \to K^+K^-$ will be always meant and reference channel will be the $B_s \to J/\psi\ \phi$ with $J/\psi \to \mu^+\mu^-$. In each dataset is available the number of events N listed in table as well. The generator cross section for each dataset σ_{gen} was computed as the cross section value from PythiaB output file multiplied by the efficiency of filter[2] that were applied during event generation. For background samples the cross section of i-th decay mode σ_i is equal to σ_{gen}, therefore it can be directly used to compute the number of expected events (will be done in section 5.3).

However, for signal and reference modes (when was one decay channel forced during the generation) σ_{gen} has to be multiplied by branching ratios of decays leading to given final state (for details see Ref. [14]). In Table 4.3 are listed branching ratios $\mathcal{B}$ of decays used to compute cross sections σ_i of signal and reference channels (values from [9] and [11]).

[2]Filters are tools accepting just events having particles with p_{T} and $|\eta|$ above selected threshold in the final state. In event generation `BSignalFilter` was used for signal, `MultiLeptonFilter` for background samples and `TestHepMC` for both. The efficiency is calculated from numbers of accepted and rejected events which are also in PythiaB output file.

Dataset	Dataset name	Tag	N	σ_{gen}[fb]	σ_i[fb]
Signal channels					
108438	PythiaB_Bs_PhiMu4Mu4	-	10^5	754×10^6	605
108440	PythiaB_Bs_PhiMu6Mu4	sig	10^5	533×10^6	427
Reference channel					
108424	PythiaB_Bs_Jpsi_mu6mu4_phi_KK	ref	5×10^4	172×10^6	13.3×10^3
Background channels					
108421	PythiaB_bbmu2p5mu2p5X	bb	10^6	546×10^6	
108463	PythiaB_ccmu2p5mu2p5X	cc	10^6	266×10^6	
108441	Pythia_DYLowBPhysM_mu2p5mu2p	DY	10^6	3.3×10^6	

Table 4.2: Datasets used for analysis, number of events N, generator cross section σ_{gen} and final cross section σ_i of i-th decay channel.

Process	$\mathcal{B}$
$B_s \to \phi\ \mu^+\ \mu^-$	1.64×10^{-6}
$B_s \to \phi\ J/\psi$	1.3×10^{-3}
$\phi \to K^+\ K^-$	0.489
$J/\psi \to \mu^+\ \mu^-$	0.0593

Table 4.3: Branching ratios of signal and reference decays subprocesses.

Chapter 5

Offline Analysis of $B_s^0 \to \phi^0 \mu^+ \mu^-$

Datasets from MC production contain information similar to real data from detector – hits, read out values and particle properties computed during processing by trigger such as momentum, charge, type of particle, probable primary particle, binary information on which triggers were passed, etc. The true information on particle level (quantities from PythiaB, real particle type, particle genealogy[1]) is stored as well, therefore these datasets are analyzed with slightly different algorithms than real data.

For offline analysis of datasets listed in Table 4.2 in previous chapter the algorithm developed by ATLAS B-physics group was used. It is a part of ATHENA package `BPhys/RareDecayAlgs` named `MC8_b2Xll` and available e.g. through interface [18]. Detailed description of B-physics tools and algorithms can be found e.g. in Ref. [19].

To improve this analysis algorithm, a tool for B-hadron tagging was added to `RareDecayAlgs` and used to tag the flavour of B_s. B-tagging algorithm and results are described in subsection 5.4.

The output of the `MC_b2Xll` algorithm is in the form of ROOT[2] n-tuples which contain a list of all possible candidates of the decay, with full information on each part of the decay tree down to the tracks. Final analysis is than being performed on these ROOT n-tuples using ROOT script. The general technique is therefore to keep cuts in the ATHENA offline analysis algorithm as broad as possible and use n-tuples for detailed study of cut efficiencies.

5.1 Offline Analysis Settings

Having available the true information about particles generated in each event, it is possible to study the performance of various settings of analysis algorithm.

In Figure 5.1 are shown the invariant mass spectra of di-muons after offline analysis of signal dataset using true information (left) and using combined signal from muon chambers and Inner detector (right). The right histogram contains

[1] Terms as mother and grandmother particle are usually used in this context.

[2] ROOT is an object-oriented data analysis framework, for details see Ref. [20].

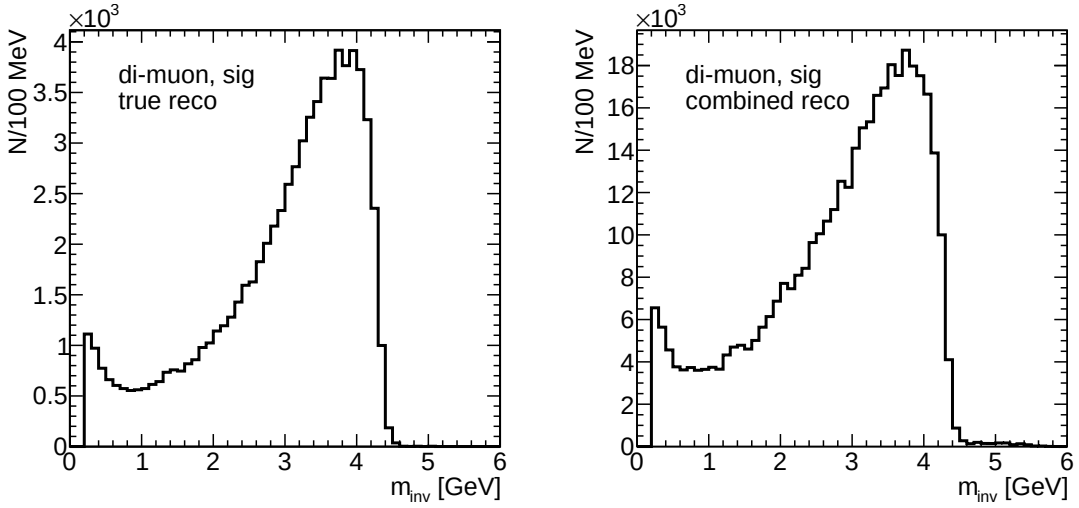

Figure 5.1: Invariant mass spectra of di-muon candidates from offline analysis using true information (left) and combined signal from muon chambers and Inner detector (right) for signal decay $B_s \to \phi\mu\mu$.

all di-muon candidates originated from decay of B_s-candidate (often more than one B_s candidate per event), while in the left one there are true di-muons from B_s decay reconstructed by algorithm, i.e. maximum 1 per event. This explains the fact that in the second plot there are approximately 5 times more entries.

Just basic selection was done when plotting the histograms. The successful vertexing of di-muon, ϕ and B_s was required, what is equivalent to event flags *dim_error*, *Phi_error* and *Bs_error* equal to 0 [3]. From these spectra (and other characteristics of B_s or ϕ) it can be deduced how the algorithm based on detector information is influencing particle properties, such as shape or mean values of their distributions. This differences should be than taken into account in the analysis of real data with offline algorithm.

In order to save disk space and not to store more data than needed for signal decay analysis, it is possible to save just B-hadrons and events with some loose cuts on vertexing quality (set in jobOptions file for offline analysis, required vertexing χ^2 of B_s and ϕ lower than 10^5). This option is useful especially in the case of background analysis. In Figure 5.2 are plotted invariant mass spectra of di-muon candidates after analysis with B-hadrons saved only and good vertexing required (left) and after full analysis (right, 5000 events), both using combined detector information (there are no true signal decays in background dataset). By their comparison it is again possible to determine how this setting is changing the invariant mass spectrum.

[3] These cuts, in following called error cuts, will be applied in next selections if not said opposite.

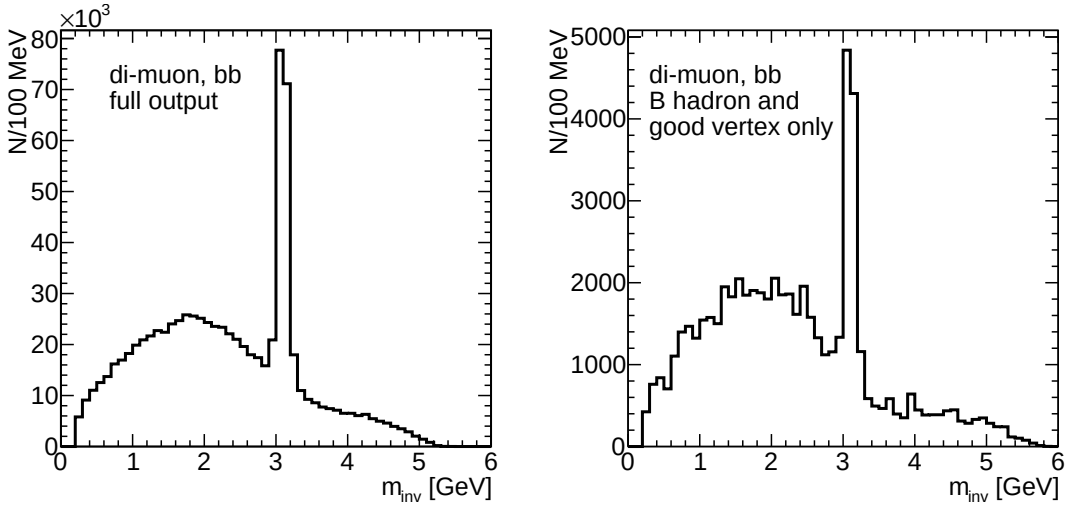

Figure 5.2: Di-muon invariant mass spectra analyzed with B-hadrons saved only and good vertexing requirement (left) and after full dataset analysis (right, 5000 events) for $b\bar{b}$ background (with combined detector information).

5.2 Signal and Background Particle Properties

For measurements of the rare decay $B_s \to \phi\ \mu^+\mu^-$ is important to select events with the highest possible efficiency and, if possible, also to completely reject background. One of the useful ways to find selection criteria and cut values is the release of some cuts (e.g. enlarge the B_s-hadron mass widow) to increase statistics and than study the influence of other cuts on background, as well as cut correlations. Most of the cut values were found by this tactics or comparing the distributions of given variable in background and signal datasets.

In the analysis of $B_s \to \phi\ \mu^+\mu^-$ will be useful to compare the influence of cuts on signal with some reference channel. As was mentioned before, the decay $B_s \to \phi\ J/\psi$ followed by $J/\psi \to \mu^+\mu^-$ is a good candidate. It has the same decay products, topology and kinematics, but the invariant mass of muon pair is fixed. This process has higher branching ratio than signal process, so it can be used to determine signal branching ratio by measuring ratio (3.9), as well as relative selection efficiency (3.10) defined above. Di-muon invariant mass spectrum for reference decay is shown in the left part of Figure 5.3.

5.2.1 Di-muon

Invariant mass spectra of true di-muons and di-muon candidates based on detector information were shown above in Figure 5.1. In the right part of Figure 5.3 is shown the background di-muon spectrum as a sum of simulated partial background from $b\bar{b}, c\bar{c}$ and Drell-Yang weighted by their relative cross section (events for $m_{\text{inv}} < 1$ GeV in Drell-Yang dataset are missing due to PythiaB problems).

Signal di-muon spectrum is not resonant (see right plot in Fig. 5.1 and com-

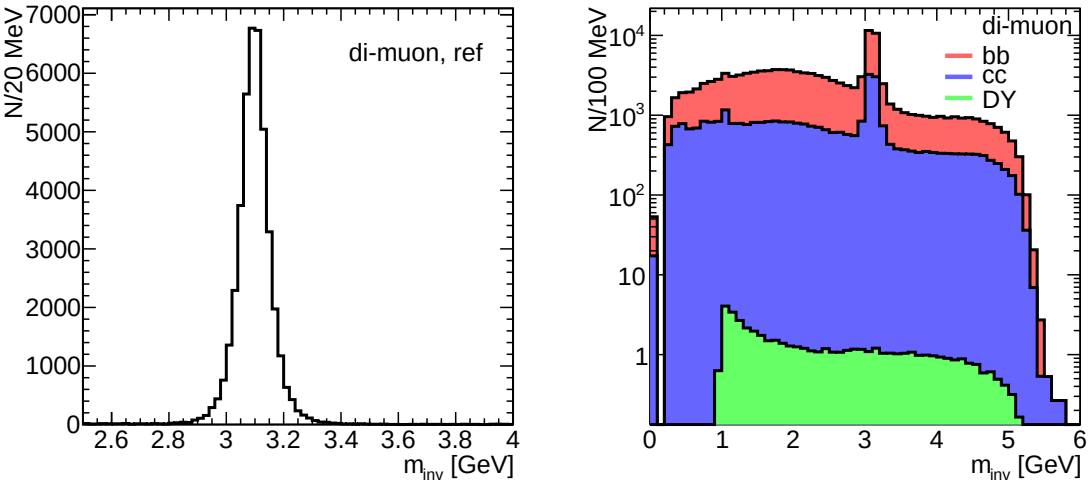

Figure 5.3: Di-muon invariant mass spectra for reference decay $B_s \to \phi\, J/\psi$ (left) and the stacked histogram of $b\bar{b}$, $c\bar{c}$ and Drell-Yang background (right).

pare with resonant spectrum of reference decay in left panel of Figure 5.3), therefore just kinematic and data quality cuts can be applied (in following text refered as di-nuon cut subset):

- muon $p_{\mathrm{T}} \geq 4$ GeV for both muons or 4 GeV for one muon and 6 GeV for the second (depending on the cut used during simulation of dataset)
- di-muon $|\eta| \leq 2.5$ to respect the high acceptance region of Inner detector
- di-muon invariant mass in kinematically accessible region $(2m_\mu, m_{B_S} - m_\phi)$
- excluding di-muon invariant mass equal to PDG mass of $c\bar{c}$ resonances $J/\psi, \psi(2\mathrm{S})$ and 3σ window around: $(3096.92 \pm 3 \cdot 54)$ MeV for J/ψ and $(3686.09 \pm 3 \cdot 60)$ MeV for $\psi(2\mathrm{S})$ to suppress background
- di-muon vertex quality $\chi^2/NDoF \leq 3$ [4], see left plot in Fig. 5.4, where are shown the normalized[5] $\chi^2/NDoF$ distributions for signal and background samples[6].
- sum of hits in Pixel detector and SCT higher than 6 for each muon

Parameter σ for width of J/ψ mass window was chosen by fitting a Gaussian distribution to the invariant mass of di-muons in reference channel, see left plot

[4] NDoF – N Degrees of Freedom.

[5] Normalized distribution in this context means normalized to 1×number of events in the smaller dataset, i.e. signal.

[6] Because of the highest gain from $b\bar{b}$, just distributions of variables from this dataset will be compared with signal to illustrate the choice of cut values. Samples on $c\bar{c}$ and Drell-Yang production were studied by optimization of cut efficiency and are summarized in subsection 5.3

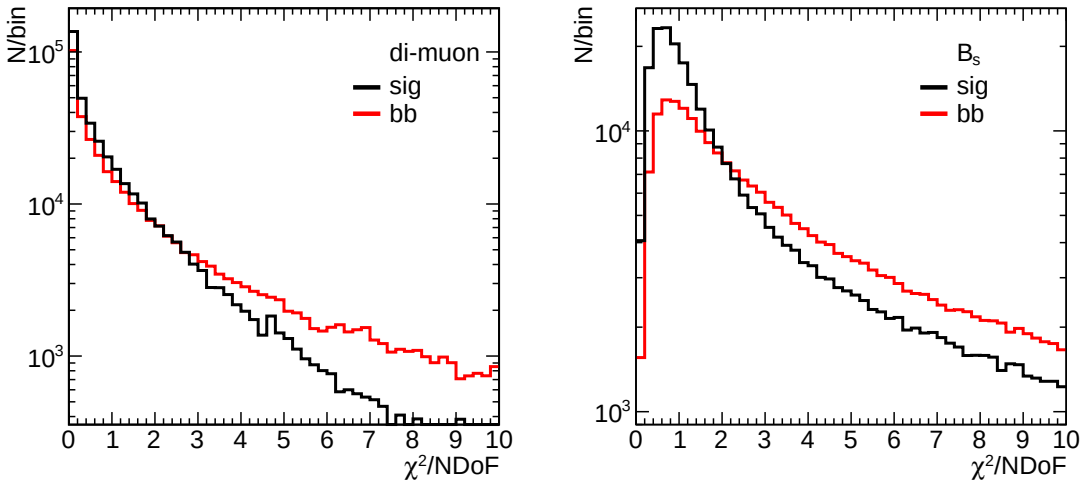

Figure 5.4: Vertex quality $\chi^2/NDoF$ of di-muon (left) B_s candidates (right) for signal and background dataset (red).

in Fig. 5.3. Due to the fact that the peak corresponding to ψ is not visible in background spectrum, the value of σ was chosen taking into account that the detector resolution is worse for higher particle mass, while the full width $\Gamma_{\psi(2S)}$ = 309 keV can be neglected.

5.2.2 K^+, K^- and ϕ-mesons

$K^\pm$ mesons are not clearly identified by the Inner detector and calorimeter system[7], therefore any track which was not identified as muon is included into the analysis. Excluding muons can suppress e.g. background events with semileptonic decay of charmed mesons.

In the offline analysis are computed two similar variables. The first of them, *invariant mass*, is the invariant mass of ϕ-candidate before vertexing and cut in this step of offline analysis is saving time by not reconstructing candidates with mass evidently different from mass of particle. The selection window around PDG value of ϕ mass is wider due to the fact that in the beginning of analysis the track parameters are given with respect to IP and invariant mass of particle which decayed in secondary vertex is therefore different than its real value. During vertexing is computed the corrected value *mass* and tighter cut can be applied. This method is used also in reconstruction of B_s vertex and two cuts on mass are given.

In total, these $K^\pm$ and ϕ cuts were applied:

- kaon $|\eta| \leq 2.5$ (acceptance of Inner detector)

[7]In fact, some methods for particle identification using energy losses in inner detector or other variables are implemented, but in this analysis are the cut on invariant mass of ϕ and latter event selection excluding other particles with reasonable efficiency.

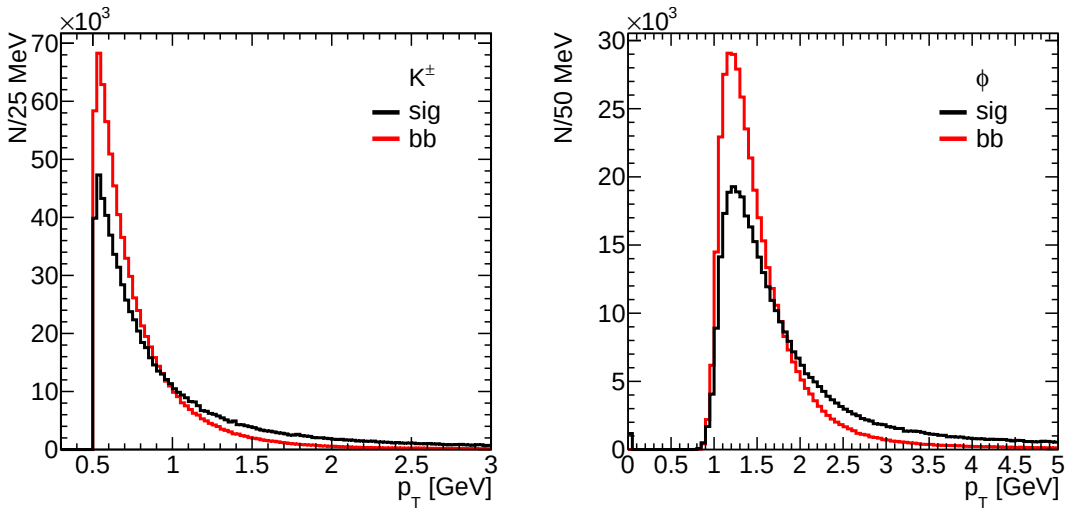

Figure 5.5: Transverse momentum distributions for $K^{\pm}$ (left) and ϕ candidates (right) for signal and background dataset (red).

- kaon $p_{\mathrm{T}} \geq 1$ GeV (left panel in Fig. 5.5)
- sum of kaon hits in Pixel detector SCT higher than 6
- mass of ϕ in the range of (1020 ± 10) MeV, invariant mass (1020 ± 20) MeV
- ϕ-meson $p_{\mathrm{T}} \geq 1.8$ GeV (see right plot in Fig. 5.5)
- ϕ vertexing quality $\chi^2/NDoF \leq 3$

5.2.3 B_s-meson

The selection of B_s-candidates is very similar to ϕ but for adding the proper time cut. The often used cut on B_s momentum pointing to the interaction point (within some interval around it) is not needed, because it is applied during B_s vertexing.

For B_s selection are used following cuts:

- mass in the (5366.3 ± 70) MeV interval, invariant mass (5366.3 ± 200) MeV (the difference between variables was explained above)
- $p_{\mathrm{T}} \geq 12$ GeV (see right plot in Fig. 5.6)
- proper time $\tau \geq 0.7$ ps (left panel in Fig. 5.6)
- vertexing quality $\chi^2/NDoF < 2$ (right plot in Fig 5.4)

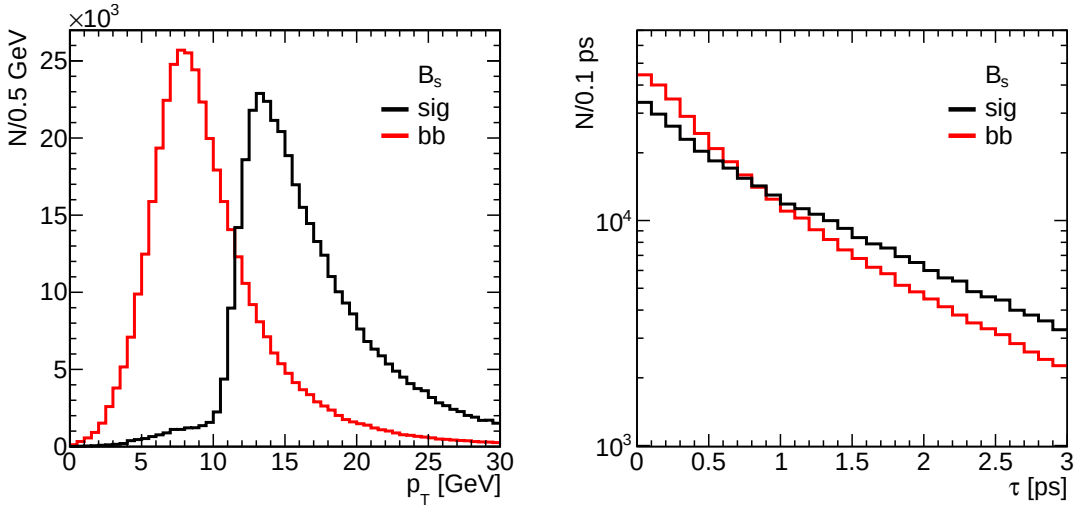

Figure 5.6: B_s transverse momentum p_{T} (left) and proper time τ distribution (right) for signal and background (black and red respectively).

5.3 Selection Efficiency

All cut subsets and their signal and background efficiencies are listed in Table 5.3, together with the total selection efficiencies for each channel. The number of detected events N_i, that is expected for i-th decay channel using selection algorithm described in previous chapters with given cuts (decays of both B_s and $\bar{B}_s$), is computed as

$$N_i = \mathcal{L}_{\mathrm{int}}\ \sigma_i\ \varepsilon_i\ S\ , \tag{5.1}$$

where $\mathcal{L}_{\mathrm{int}} = 30\ \mathrm{fb}^{-1}$ is the integrated luminosity (corresponds to approximately three year of LHC operation at luminosity $\mathcal{L} = 10^{33}\mathrm{cm}^{-2}\mathrm{s}^{-1}$), σ_i is the cross section of given process from Table 4.2, ε_i is the selection efficiency for given channel and $S = 2$ is the symmetry factor taking into account the decays of $\bar{B}_s$, for background channels is $S = 1$.

Equation (5.1) can be used for measurement of branching ratio and other quantities, which have the same values for particles and antiparticles. For variables such as $\mathcal{A}_{\mathrm{FB}}$ should be used $S = 1$ with the efficiency of B-tagging included.

Due to the limited number of events in data samples the selection efficiency for background has been found zero. Assuming that background events follow a Poisson distribution, the upper limit of mean value can be found by Neyman procedure (see e.g. Ref. [11]) giving a result an upper limit $N_{\mathrm{up}} = 3$ at 95% CL.

The value of relative acceptance defined in (3.10) for signal and reference channel is

$$A_{\mathrm{rel}} = \frac{\varepsilon_{J/\psi\phi}}{\varepsilon_{\mu^+\mu^-\phi}} = \frac{\varepsilon_{\mathrm{ref}}}{\varepsilon_{\mathrm{sig64}}} = \frac{10.89\%}{7.686\%} = 0.142\ . \tag{5.2}$$

Cut subset	$\varepsilon_{\text{sig64}}[\%]$	$\varepsilon_{\text{sig44}}[\%]$	$\varepsilon_{\text{ref}}[\%]$	$\varepsilon_{bb}[\%]$	$\varepsilon_{cc}[\%]$	$\varepsilon_{\text{DY}}[\%]$
di-muon	53.65	52.62	77.29	1.196	0.733	0.042
kaons	95.36	87.81	36.78	5.337	5.376	0.125
ϕ	72.06	68.73	29.81	3.318	3.359	0.108
B_s	43.02	37.29	15.50	0.099	0.055	0
all cuts	7.686	6.503	10.89	0	0	0
N	1968	2361	86901	< 49000 95% C.L	<24000 95% C.L.	< 300 95% C.L.

Table 5.1: Efficiencies of the sub-sets of cuts described in subsection 5.2. For signal decay $\varepsilon_{\text{sig64}}$ (dataset 108440) and $\varepsilon_{\text{sig44}}$ (dataset 108438), ε_{ref} for reference channel (cut on J/ψ mass is removed) and background: ε_{bb} for $b\bar{b}$, ε_{cc} for $c\bar{c}$ and Drell-Yang production ε_{DY}. The numbers of expected events N in data with integrated luminosity 30 fb^{-1} are computed using Equation 5.1.

Trigger	$\varepsilon_{\text{sig64}}[\%]$	$\varepsilon_{\text{sig44}}[\%]$	$\varepsilon_{\text{ref}}[\%]$
trig1_L1_2MU0	5.26	4.25	7.15
trig1_L1_2MU0_MU6	5.20	4.16	7.11
trig2_L2_2mu4_DiMu	4.22	3.45	6.07
trig3_EF_2mu4_DiMu	4.04	3.28	5.68
N (trig3_EF_2mu4_DiMu)	1034	1191	45326

Table 5.2: Efficiencies of event selection with all cuts applied together with di-muon triggers for signal channel $\varepsilon_{\text{sig64}}$ and $\varepsilon_{\text{sig44}}$, ε_{ref} for reference channel (cut on J/ψ mass is removed) and the number of expected events after integrated luminosity 30 fb^{-1} N.

5.3.1 Trigger Efficiency

The selection efficiencies after applying all cuts and requesting the event to pass some of di-muon triggers used in B-physics are shown in Table 5.3.1 as an example for few of them. The efficiency of background events suppression by applying all cuts is assumed to be equal to 1 before using triggers, therefore these datasets are not included here. The real number of observed events is depending on which triggers we select, therefore following analysis will be done without triggers.

5.4 B-meson Flavour Tagging

As B_s and $\bar{B}_s$ have the same decay modes, it is not possible to identify which one of them was the primary particle just from parameters of reconstructed ϕ and muon pair. The uncertainty of B-hadron flavour at production has influence on measurement of many quantities, e.g. in studies of CP-violation, mixing or the forward-backward asymmetry important for new-physics searches.

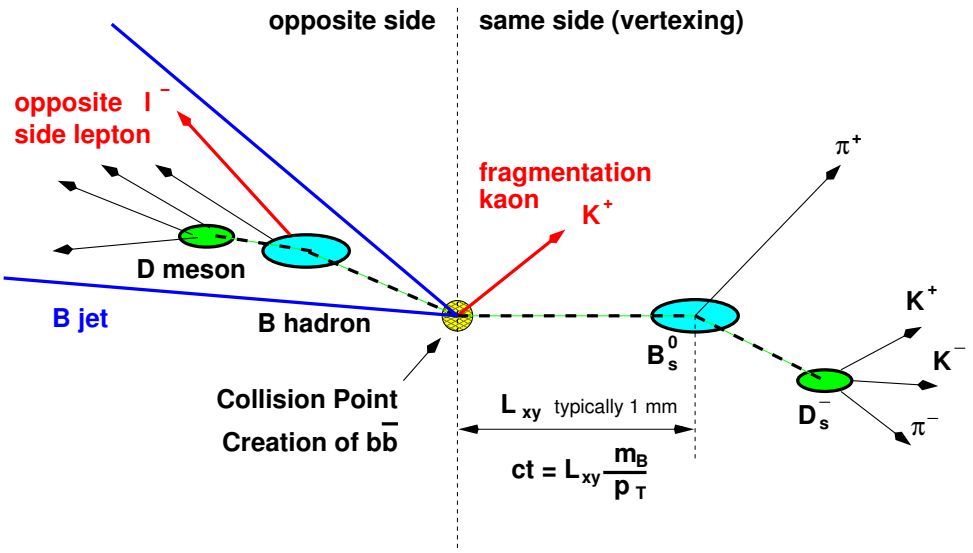

Figure 5.7: Schema of typical flavour tagging methods, taken from [21].

There are more flavour tagging algorithms, their principle is illustrated in Figure 5.7, where is shown a typical topology of event with B-decay. One of possibilities how to determine flavour of the B-meson candidate is *opposite side lepton tagging* method [8] searching for the highest p_{T} lepton unassociated with the signal channel (muon or electron depending on the choice of input particle collection) assuming that this lepton originates from $b \to c\, l^-\, \bar{\nu}_l$ or $\bar{b} \to \bar{c}\, l^+\, \nu_l$ decay of the second B meson. However, this method can be used just in a small number of cases due to small branching ratio of semileptonic decays $\mathcal{B}(B \to \ell X_s) \sim 20\%$.

The second algorithm, so called *jet tagging* (opposite side), is based on calculating the total weighted charge of b-jet to find out if the jet was produced by b or $\bar{b}$-quark hadronization. The jet charge is in most cases positive for $\bar{b}$-jets and negative for b-jets. Three of the possible ways how to define the jet charge are described and studied in [5] in case of $B_s \to \phi\ J/\psi$ decay, in `MC8_b2Xll` was implemented the p_{L} method with optimized parameters. According to studies presented in the work mentioned above is the tagging efficiency $\varepsilon_{\mathrm{tag}} = (N_{\mathrm{r}} + N_{\mathrm{w}})/N_{\mathrm{t}}$ $= 62.5\%$ (the fraction of B-mesons tagged either correctly N_{r} or incorrectly N_{w} in all tagged events N_{t}) and the wrong tag fraction $w_{\mathrm{tag}} = N_{\mathrm{w}}/(N_{\mathrm{r}}+N_{\mathrm{w}}) = 37.4\%$.

If we define the dilution (or purity) as

$$D_{\mathrm{tag}} = \frac{N_{\mathrm{r}} - N_{\mathrm{w}}}{N_{\mathrm{r}} + N_{\mathrm{w}}} = 1 - 2w_{\mathrm{tag}}\ , \tag{5.3}$$

the relation between the true asymmetry $\mathcal{A}_{\mathrm{true}}$ (difference between the values of observable for particle and antiparticle normalized to their sum) and measured

[8] Both lepton and jet tagging algorithms are implemented in ATHENA package `BPhys/BPhysAnalysisTools/BFlavourCombinedTagger`.

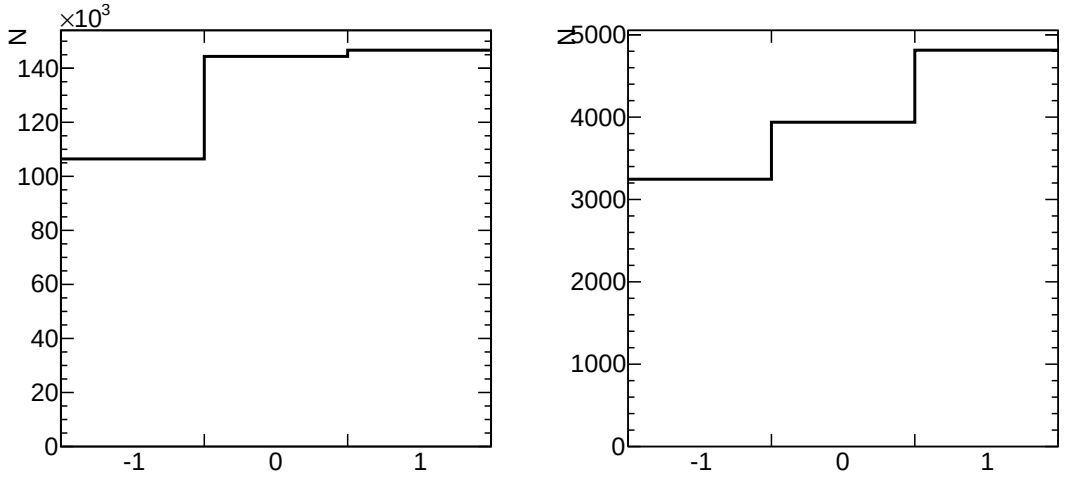

Figure 5.8: The results of jet tagging for signal decay with error cuts (left) and after all cuts applied (right).

value $\mathcal{A}_{\text{meas}}$ is given by

$$\mathcal{A}_{\text{true}} = \frac{1}{D_{\text{tag}}} \mathcal{A}_{\text{meas}} \tag{5.4}$$

and the statistical uncertainty of $\mathcal{A}_{\text{true}}$ is (in approximation for small values of asymmetry, see [5])

$$\sigma_{\mathcal{A}} \approx \frac{1}{\sqrt{\varepsilon_{\text{tag}}\ D_{\text{tag}}^2\ N_{\text{t}}}} = \frac{\sqrt{N_{\text{r}} + N_{\text{w}}}}{N_{\text{r}} - N_{\text{w}}}\ . \tag{5.5}$$

Results of jet tagging for signal decay after all cuts from previous sections applied (combined detector information, values after error cuts listed for reference) are shown in Figure 5.8. The numbers of each tag and corresponding efficiency and uncertainty of asymmetry computed with equations (5.3) – (5.5) are listed in Table 5.3. The set of B_s after error cuts is representing all B_s candidates found by offline analysis algorithm (that is why the total number of entries is $\sim$ 4-times higher than the number of events in dataset, i.e. 10^5). After applying all cuts, the set is containing just true B_s, therefore the number of mesons with tag = -1 is equal to N_{w}, tag 0 means that the tagger could not make clear decision (N_0 events) and the number of mesons tagged 1 is N_{r}.

The value of tagging efficiency ε_{tag} for B_s after all cuts applied is by 4.8% higher than the value 62.5% from [5], on the other hand the wrong tag fraction is higher by 2.85%, what leads to asymmetry uncertainty $\sigma_{\mathcal{A}} = 0.0572$. These results are computed for $\sim 12 \times 10^3$ registered events passing all cuts. The results for signal decay after 30 fb^{-1} (total number of tagged events $N_{\text{t}} = 1968$ is from Table 5.3) were computed using the same percentages of right, wrong and no tags. For this number of tagged events the asymmetry uncertainty is $\sigma_{\mathcal{A}} = 0.141$.

It is obvious that for lower statistics the asymmetry uncertainty would grow and that would strongly decrease the sensitivity of many measurements, e.g. of

Dataset	N_{w}	N_0	N_{r}	$\varepsilon_{\mathrm{tag}}$	w_{tag}	D_{tag}	$\sigma_{\mathcal{A}}$
sig, error cuts	106437	144376	146686	0.6368	0.4205	0.1590	0.0125
sig, all cuts	3238	3914	4807	0.6727	0.4025	0.1950	0.0572
sig after 30 fb^{-1}	533	644	791	0.6727	0.4025	0.1950	0.1410

Table 5.3: The numbers of right, wrong and not tagged B_s candidates for signal decay dataset (N_{w}, N_0 and N_{r} respectively), computed tagging efficiency $\varepsilon_{\mathrm{tag}}$, wrong fraction w_{tag}, dilution D_{tag} and uncertainty of asymmetry $\sigma_{\mathcal{A}}$.

CP asymmetries or mixing. However, these properties of B_s can be measured in other decays with higher branching ratios.

In case of forward-backward asymmetry the situation looks different due to the fact that $\mathcal{A}_{\mathrm{FB}}$ for antiparticle has opposite sign and the same value as $\mathcal{A}_{\mathrm{FB}}$ of antiparticle, therefore their asymmetry would be $\mathcal{A}_{\mathcal{A}_{\mathrm{FB}}} = \mathcal{A}_{\mathrm{FB}}(B_s) + \mathcal{A}_{\mathrm{FB}}(\bar{B}_s)$. In fact, if the positive tag is required during event selection, it is selecting $N_{\mathrm{r}}/(N_{\mathrm{r}} + N_{\mathrm{w}})$ fraction of B_s and $N_{\mathrm{w}}/(N_{\mathrm{r}} + N_{\mathrm{w}})$ of $\bar{B}_s$ and the measured forward-backward asymmetry has the properties needed for formulas (5.3) – (5.5) to be appropriate.

In the early data taking phase (with an integrated luminosity ~ 150 pb^{-1}), the self-tagging decays (such as $B_d^0 \to J/\psi K^{0*}$) are planned to be used to calibrate the jet charge tagging method and find its best parameters [5]. Results will also help to improve MC fragmentation models for B_s decays.

5.5 Forward-Backward Asymmetry

The influence of selection cuts described in section 5.2 on forward-backward asymmetry is illustrated in Figure 5.9. In the left graph there is shown the true $\mathcal{A}_{\mathrm{FB}}$ as a function of $s = m^2_{dimu}/m^2_{B_S}$ for signal dataset after applying error cuts. In the right part is plotted the same dependency for analysis based on combined detector information with all cuts included. Values are strongly dependent on the choice of binning.

Both distributions are fitted by linear function in the interval of growing value of $\mathcal{A}_{\mathrm{FB}}$. The point where the fit is crossing the x-axis, i.e. the value s_0 where is $\mathcal{A}_{\mathrm{FB}}$ changing sign, is one of the important observables (less affected by theoretical uncertainties). The values are $s_0 = (0.117 \pm 0.007)$ for true distribution and $s_0 = (0.118 \pm 0.024)$ for the second fit. The uncertainty of measuring $\mathcal{A}_{\mathrm{FB}}$ depends on the resolution of $\cos(\theta)$ (θ is the angle between momenta of B_s and μ^+) which is ~ 0.01. That leads to resolution of $\mathcal{A}_{\mathrm{FB}} \sim 0.013$, therefore in both plots was used just statistical error which is higher for data after cuts (less events). Higher difference of asymmetry value and high statistical error of some bins is caused by smaller number of events after mass cuts ($s = 0.33$ is the center of J/ψ mass window, $\psi(2S)$ corresponds to $s = 0.47$) or at the end of kinematically allowed di-muon mass region. After excluding these bins from analysis the shape of distribution is similar to the true values.

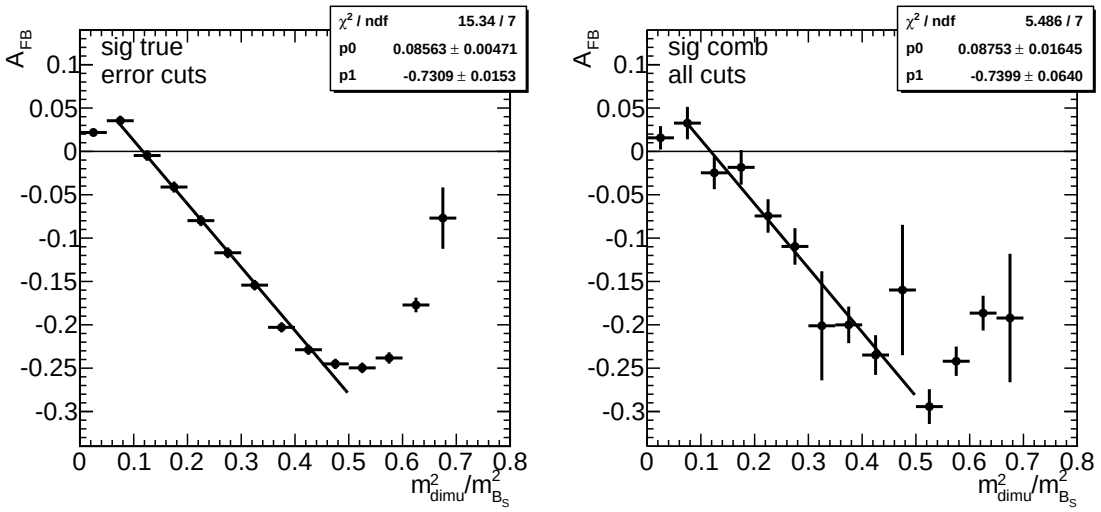

Figure 5.9: The true forward-backward asymmetry $\mathcal{A}_{\rm FB}$ as a function of $m^2_{dimu}/m^2_{B_S}$ with error cuts (left) and results of analysis based on combined detector information after all cuts applied (right). The parameters of linear fit are also shown in panels.

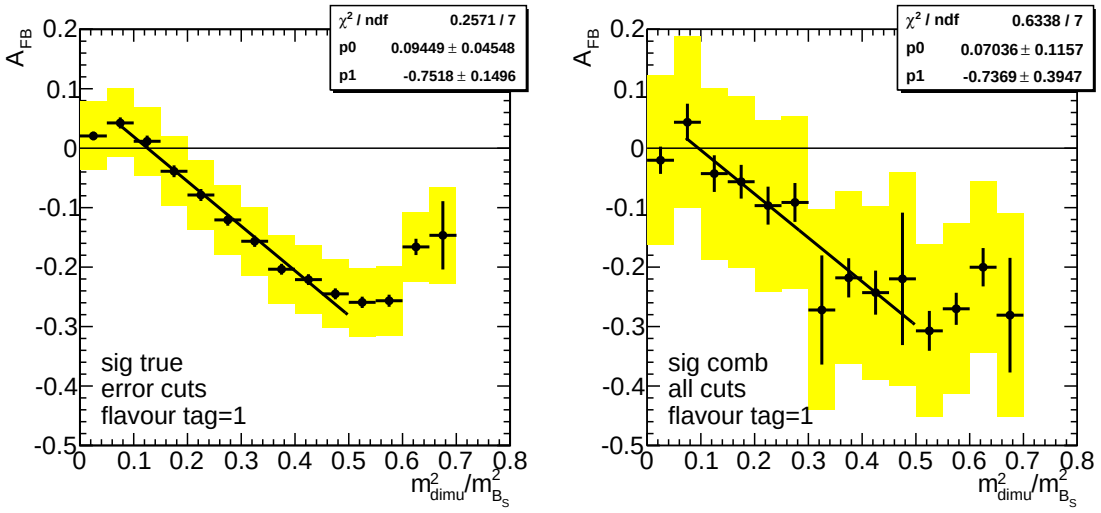

Figure 5.10: The true forward-backward asymmetry $\mathcal{A}_{\rm FB}$ as a function of $m^2_{dimu}/m^2_{B_S}$ with error cuts and tagging (left) and results of analysis based on combined detector information after all cuts applied and requiring flavour tag = 1 (right). In both plots the black error bars represent the statistical errors, yellow rectangles are combining statistical error and error of tagging $\sigma_{\mathcal{A}}$ from Table 5.3.

The same dependencies as above including flavour tagging are shown in Figure 5.10. In the left plot there are results of analysis based on true information with tagging, in the right are shown data representing detector-based analysis after selection and tagging for integrated luminosity 30 fb^{-1} (choice of the number of events influences errors). Values of $\mathcal{A}_{\mathrm{FB}}$ are the same as in previous plots[9]. Error without including tagging uncertainty are drawn by black bars, while yellow areas are representing the error combined from statistical error and error of tagging (values of tagging $\sigma_{\mathcal{A}}$ from Table 5.3). The real data without background (assuming flat $\mathcal{A}_{\mathrm{FB}}$ of background data) should look like the right plot with yellow error bars. As before, distributions are fitted by linear function with results shown in plots, values of s where $\mathcal{A}_{\mathrm{FB}}$ changes sign are $s_0 = (0.126 \pm 0.066)$ for left plot and $s_0 = (0.095 \pm 0.166)$ for distribution after selection and tagging. Removing two bins around J/ψ and $\psi(2\mathrm{S})$ changes the result to $s_0 = (0.107 \pm 0.176)$.

The measurement of forward-backward asymmetry $\mathcal{A}_{\mathrm{FB}}$ can be a good test of CP symmetry. Without flavour tagging and with flat asymmetry of background the measured $\mathcal{A}_{\mathrm{FB}}$ should be equal to zero.

5.6 Physical Quantities after Selection

Di-muon invariant mass spectrum after selection with all cuts is shown in left panel of Figure 5.11, for comparison also the spectrum with error cuts is plotted in the same histogram. The major part of distribution did not change the shape except of gaps after removing invariant mass equal to mass of J/ψ and $\psi(2\mathrm{S})$. In the right part of figure is shown a similar plot for reference channel with peak of J/ψ passed selection criteria.

In Figure 5.12 are plotted invariant masses of B_s and ϕ passed all selection cuts. Distributions are fitted by Gaussian function and its parameters are listed in plots.

[9]For real data it will be computed from measured $\mathcal{A}_{\mathrm{meas}}$ using Equation 5.4.

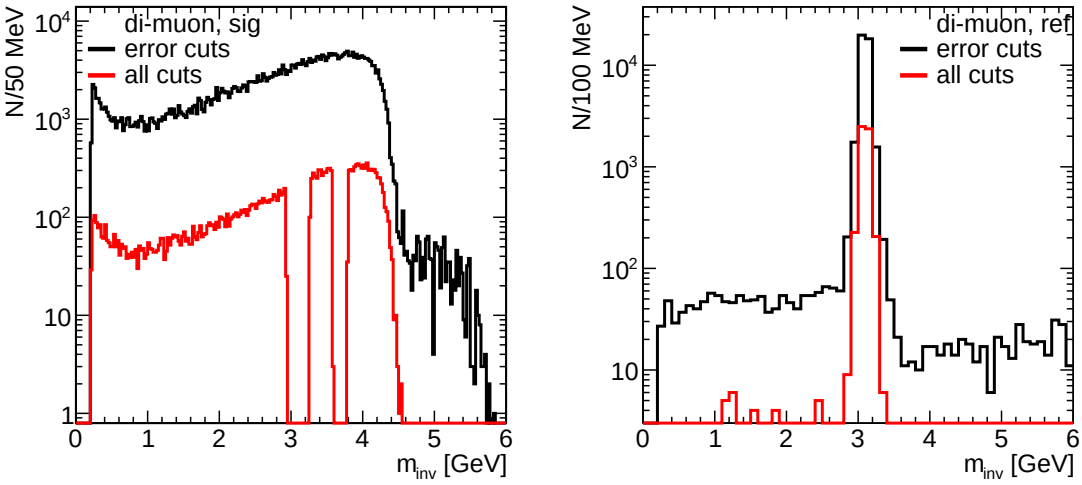

Figure 5.11: Invariant mass spectra of di-muon candidates for signal (left) and reference channel (right). For both datasets are spectra with basic error cuts painted in black, in red are spectra after all cuts applied.

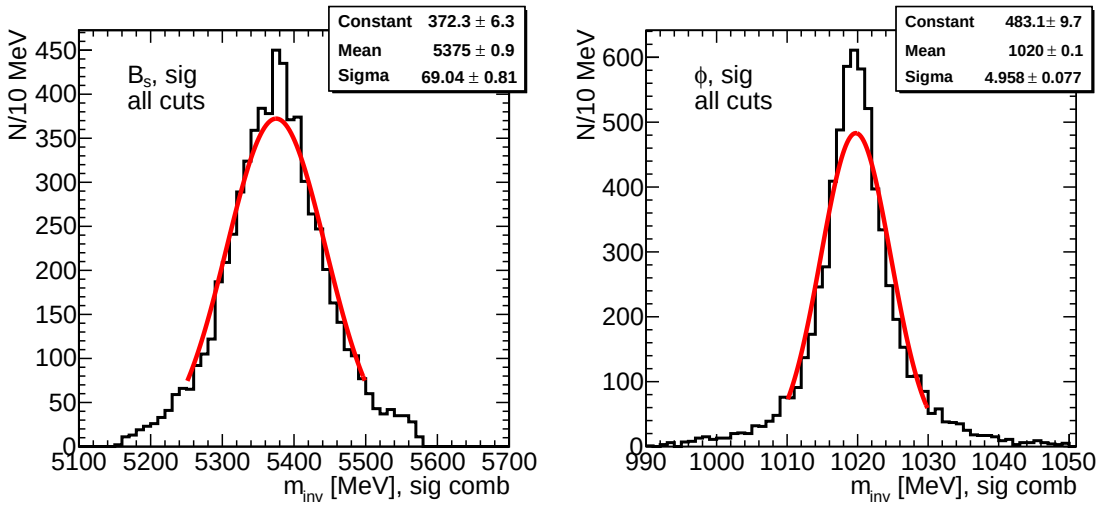

Figure 5.12: Invariant mass spectra of B_s (left) and ϕ-candidates (right) after all selection cuts. Distributions are fitted by Gaussian, the fit parameters are listed in boxes.

Chapter 6

Conclusions

In this thesis the ATLAS detector at CERN was described and an introduction to the theoretical framework of rare decays of beauty hadrons was given. The most interesting observable quantities for these decays are the branching ratio, differential di-muon invariant mass and the forward-backward asymmetry, which are highly sensitive to BSM signatures.

A more detailed theoretical base of semileptonic rare decay $B_s^0 \to \phi^0 \mu^+ \mu^-$ was presented, together with methods of its detection and possible background sources. After a short description of the Monte Carlo data simulation and analysis framework on ATLAS experiment the results of the offline analysis were presented. The cuts for event selection were found and optimized by comparing distributions of variables for simulated signal and background data and considering kinematics, detector properties and other conditions. Values are presented in section 5.2. The selection efficiencies and the background rejection factors for subsets of cuts are shown in Table 5.3 along with a number of expected events in data with integrated luminosity 30 fb^{-1} for signal event and three background channels ($b\bar{b}, c\bar{c}$ and Drell-Yang production of final state $\mu\mu X$). Due to the limited number of events in data samples the selection efficiency for background has been found to be zero and the upper limit on the number of background events at CL 95% was computed.

The selection criteria were applied also on reference channel $B_s \to J/\psi\ \phi$ with $J/\psi \to \mu^+\mu^-$ and the value of relative selection acceptance $A_{\mathrm{rel}} = 0.142$ was computed.

The flavour tagging was described and the jet charge tagging method was studied and applied on the forward-backward asymmetry measurement. The value of $s = m^2_{dimu}/m^2_{B_S}$ where asymmetry changes sign is one of observables less influenced by theoretical uncertainties, its values were computed for data from true analysis and for data from detector-based analysis with jet tagging and selection cuts applied. The error of measurements is strongly dependent on the number of detected events and tagging efficiency.

The plots in the two last subsections show that the offline analysis cuts do not change the shape of the di-muon mass spectrum and the forward-backward

asymmetry distribution and the resolutions of mass measurement are 69 MeV for B_s and 5 MeV for ϕ.

In many cases statistical errors of results were not computed. This was done because of the fact that statistical errors can be neglected in comparison with uncertainties given by theoretical error of $b\bar{b}$ production rate at high energies (the error is practically 100%). This cross section has to be measured in early stage of operation. Systematic errors such as tracking, particle identification or tagging efficiency may also have an influence on the number of registered events and observed spectra. Better results may be achieved after enough time of the LHC operation, when the detector will be fully understood and models for data simulation will be adjusted using early data.

Bibliography

[1] O. Bruning (Ed.) *et. al.*, *LHC design report. Vol. I: The LHC main ring*, CERN-2004-003-V-1

[2] F. Gianotti f. t. ATLAS Collaboration: *ATLAS status and highlights*, talk at ICHEP 2010

[3] W. W. Armstrong *et al.* [ATLAS Collaboration], *ATLAS Technical Proposal for a General Purpose p-p Experiment at the Large Hadron Collider at CERN*, CERN/LHCC/94-43

[4] ATLAS Collaboration, *ATLAS: Detector and physics performance technical design report*, Volumes I, II, CERN/LHCC 99-14 and CERN/LHCC 99-15

[5] G. Aad *et al.* [The ATLAS Collaboration], *Expected performance of the ATLAS experiment : detector, trigger and physics*, CERN-OPEN-2008-020, arXiv:0901.0512 [hep-ex]

[6] ATLAS Collaboration, *ATLAS High-level trigger, data-acquisition and controls: Technical Design Report*, CERN/LHCC/2003-022

[7] N. Nikitine, P. Reznicek, S. Sivoklokov, M. Smizanska and K. Toms, *Potential of Rare B-decays in ATLAS*, Nuclear Physics B (Proc. Suppl.) **163** (2007) 147-152

[8] P. Ball *et al.*, *B Decays at the LHC*, CERN-TH/2000-101

[9] C. Q. Geng and C. C. Liu, *Study of $B_s \to (\eta,\ \eta',\ \phi)\ell\bar{\ell}$ decays*, J. Phys. G **29**, 1103 (2003) [arXiv:hep-ph/0303246]

[10] H.-M. Choi, *Light-Front Quark Model Analysis of Electroweak Decays of Pseudoscalar and Vector Mesons*, Ph.D. thesis [arXiv:hep-ph/9911271]

[11] C. Amsler *et al.* [Particle Data Group], *Review of particle physics*, Phys. Let. B667, 1 (2008) and 2009 partial update for the 2010 edition, http://pdg.lbl.gov

[12] H. Miyake, f. t. CDF and t. D. Collaborations, *Rare decays / B_s CPV measurements at Tevatron*, PoS **HCP2009**, 033 (2009), [arXiv:1003.0164 hep-ex]

[13] V. M. Abazov *et al.* [D0 Collaboration], *S*earch for the rare decay $B_s^0 \rightarrow \phi\ \mu^+\mu^-$ with the D0 detector, Phys. Rev. D **74**, 031107 (2006) [arXiv:hep-ex/0604015]

[14] M. Smizanska, *PythiaB: interface to Pythia6 dedicated to simulation of beauty events*, ATL-COM-PHYS-2003-038

[15] T. Sjostrand, S. Mrenna and P. Z. Skands, *PYTHIA 6.4 Physics and Manual,* JHEP **0605**, 026 (2006) [arXiv:hep-ph/0603175]

[16] S. Agostinelli *et al.* [GEANT4 Collaboration], *GEANT4–a simulation toolkit*, Nucl. Instrum. and Methods A **506** (2003), pp. 250-303

[17] The Athena homepage, http://twiki.cern.ch/twiki/bin/view/Atlas/AthenaFramework

[18] http://atlas-sw.cern.ch/cgi-bin/viewcvs-atlas.cgi/offline/PhysicsAnalysis/BPhys

[19] C. Anastopoulos *et al.* [ATLAS Collaboration], *Physics Analysis Tools For Beauty Physics In Atlas*, J. Phys. Conf. Ser. **119** (2008) 032003

[20] R. Brun *et al.*, *ROOT: an Object-Oriented data analysis framework, User Guide 5.26*, http://root.cern.ch/drupal/content/users-guide

[21] M. Antonelli *et al.*, *Flavor Physics in the Quark Sector*, arXiv:0907.5386 [hep-ph].

[22] A. Dewhurst *et al.*, *Low p_{T} muon and di-muon rates in ATLAS*, ATL-COM-PHYS-2007-089